Thermal Management of Li-ion batteries by Thermal Barrier Coatings

Master's thesis in Materials Engineering

Nagarajan Kumaresan

DEPARTMENT OF INDUSTRIAL AND MATERIALS SCEINCE

CHALMERS UNIVERSITY OF TECHNOLOGY
Gothenburg, Sweden 2021
www.chalmers.se

MASTER'S THESIS 2021

Thermal Management of Li-ion batteries by Thermal Barrier Coatings

Nagarajan Kumaresan

CHALMERS
UNIVERSITY OF TECHNOLOGY

Department of Industrial and Materials Science
Division of Materials and Manufacturing
CHALMERS UNIVERSITY OF TECHNOLOGY
Gothenburg, Sweden 2021

Thermal Management of Li-ion batteries by Thermal Barrier Coatings

Nagarajan Kumaresan

Supervisor & Examiner: Uta Klement, Chalmers
Company Supervisor: Karolina Länta, UBPM, Scania

Master's Thesis 2021
Department of Industrial and Materials Science
Division of Material and Manufacturing
Chalmers University of Technology
SE-412 96 Gothenburg
Telephone +46 31 772 1000
Gothenburg, Sweden 2021

Abstract

Electrification is the new normal of the upcoming world. Electrified vehicles require a system to store the electrical energy and Li-ion battery systems are one of the top contenders for energy storage because of their high power densities and repeatability in charging and discharging of the battery. Need for increasing the efficiency of the Li-ion batteries requires close packing of the cells in the battery which results in difficulties in thermal management of the Li-ion batteries. The objective of the thesis work is to experimentally verify if Thermal Barrier Coatings (TBC) can be used for preventing the thermal propagation in the Li-ion batteries and thereby stopping the accidents in electric vehicles owing to Thermal Runaway (TR). Yttria Stabilised Zirconia (YSZ) is coated on aluminium plates by Atmospheric Plasma Spraying (APS) and Suspension Plasma Spraying (SPS). The two coatings are tested thermally and mechanically, and the results are compared. APS coating shows better mechanical properties due to the presence of the polymer filling the pores in the coating whereas, the SPS coating shows better thermal properties.

Keywords: Atmospheric Plasma Spraying (APS), Suspension Plasma Spraying (SPS), YSZ, Thermal Runaway.

Acknowledgements

I would like to convey my heartfelt thanks to my examiner and supervisor from my university, Uta Klement for her patience, encouragement, and the support that she offered me for completion of my thesis work. The motivation that was offered when my back was against the wall is commendable.

I would like to express my sincere gratitude to Karolina Länta, my supervisor from Scania for endorsing and helping during my hardships and boosting my morale during the journey.

I would like to thank Anders Thibblin and Sharifi Tiva for the knowledge that they shared during the course of my time at Scania and the supporting hands that helped me complete my thesis work.

Finally, a big thanks to my friends and family for being there for me all the time.

Nagarajan Kumaresan, Gothenburg, December 2021.

Contents

1

Introduction

In today's world, transportation sector is rapidly growing, with the growth of the transportation sector, greenhouse gas emission increases polluting the air we breathe. According to the official European Union (EU) website, the major greenhouse gas that is emitted is the Carbon Dioxide (CO_2) and Light Duty Vehicles (LDV) like passenger cars and vans constitute for around 12.5% of the total EU emission of CO_2 and the Heavy-Duty Vehicles (HDV) including lorries, buses and coaches contribute 6%. To reduce the emission of this greenhouse gas, EU adopted regulations and fixed the EU fleet-wide CO_2 emission targets for passenger vehicles for the period of 2020-2024 to be 95 g CO_2/km for cars and 147 g CO_2 /km for vans. The emissions become stringent for the following years accounting to 15% reduction from 2025 and 37.5% reduction from 2030 for cars, and 15% reduction from 2025 and 31% from 2030 for vans. Failing to abide by the standards will result in huge penalties of €95 per g/km of target exceedance for LDV and €4,250 per gCO_2/tkm for HDV *[1]*. The automotive industry is shifting towards electrical power trains and hybrid vehicles to achieve the emission targets set by the EU. Lithium-ion (Li-ion) batteries are one of the top contenders for energy storage owing to its high energy and higher power densities *[2]* than compared to lead-acid and Ni-MH batteries and excellent cycling performance during charging and discharging of the batteries.

Energy saving and efficient usage of the available energy source has become the aphorism of the new and the upcoming world. Li-ion batteries comprise of individual cells stacked to form a battery module and several batteries are stacked to achieve the desired range for the vehicle. The demand for light weight vehicles and efficient power output has ensured the close packing of the cells in the batteries. The close packed arrangement has impacts on the thermal management of the batteries. If a cell is under thermal, electrical, or mechanical abuse, the cell increases its temperature rapidly. This local excessive temperature rise in Li-ion batteries may lead to thermal runaway (TR) of individual cells or an entire battery pack. The rapid increase in temperature can lead to fire hazards with smoke and explosion. There are many cases of electric vehicle explosions reported in the past *[3-7]*. The details of the accidents are given in Table 1. These accidents can be categorised into thermal abuse, electrical abuse or mechanical

abuse and the classification is given in Table 2. The different primary causes led to TR of batteries and resulted in explosion in some cases.

S. No.	Date	Location	Vehicle	Possible Cause
1	June, 2008	Columbia, US	Modified Pirus	Battery overheating *[4]*
2	May, 2011	Burlington, US	Chevy Volt	Coolant damage *[5]*
3	May, 2012	Shenzhen, China	BYD E6 taxi	Collision created high voltage circuit and ignited 25% cells.
4	Jan, 2013	Boston, US	Boeing 787	Internal short circuit *[6]*
5	Jan, 2013	Takamatsu, Japan	Boeing 787	Internal short circuit *[7]*
6	Oct, 2013	Seattle, US	Tesla model S	Short circuit occurred and ignited some cells
7	April, 2015	Shenzhen, China	Wuzhou Dragon Ev bus	Overcharging of the battery Pack to TR
8	Jan, 2016	Gjerstad, Norway	Tesla model S	Short circuit during charging.
9	April, 2016	Shenzhen, China	Wuzhou Dragon Ev bus	Short circuit caused by wire deterioration
10	June, 2016	Beijing, China	iEV5	Overheat caused by loose connection
11	July, 2016	Nanjing, China	EV Bus	Water immersion brought short circuit

Table 1: List of accidents due to Thermal Runaway of Li-ion batteries from year 2008 to 2016

Accident No.	Type of Abuse
1, 7	Thermal abuse
2, 3, 10, 11	Mechanical abuse
4, 5, 6, 8, 9	Electrical abuse

Table 2: Classification of the accidents based on the cause

1.1 Thesis Objective:

The aim of this project is to find out the mechanisms that can prevent thermal propagation and delay the thermal runaway of batteries. In addition, it should also be investigated experimentally whether thermal barrier coatings (TBC) can be used for TR prevention.

2

Lithium-Ion Batteries

Electrochemical energy is obtained from the conversion of stored chemical energy to electrical energy. The chemical reaction between the reagents through redox reactions (a combination of reduction and oxidation reactions) converts the chemical energy into electrical energy. This electrochemical energy can be obtained from batteries and fuel cells. The classification can be seen in Figure 1. Fuel cells provide the electrochemical energy by converting the chemical energy of the fuel and an oxidizing agent to electrical energy through the redox reactions in the cell. The reactions will sustain as long as the fuel (chemical consumed at the anode) is supplied from the outside. The main difference between the primary and secondary cell is that in primary cell, when the initial reactants are exhausted, the primary cell's useful life will be over. In contrast, the secondary cells can be recharged to trigger the reverse reactions and can be used indefinitely. Batteries consist of anode, cathode, and electrolyte. In the case of primary batteries, the cathode and anode are not interchanged during the charging and the discharging cycles, but in secondary batteries the cathode and anode are interchanged.

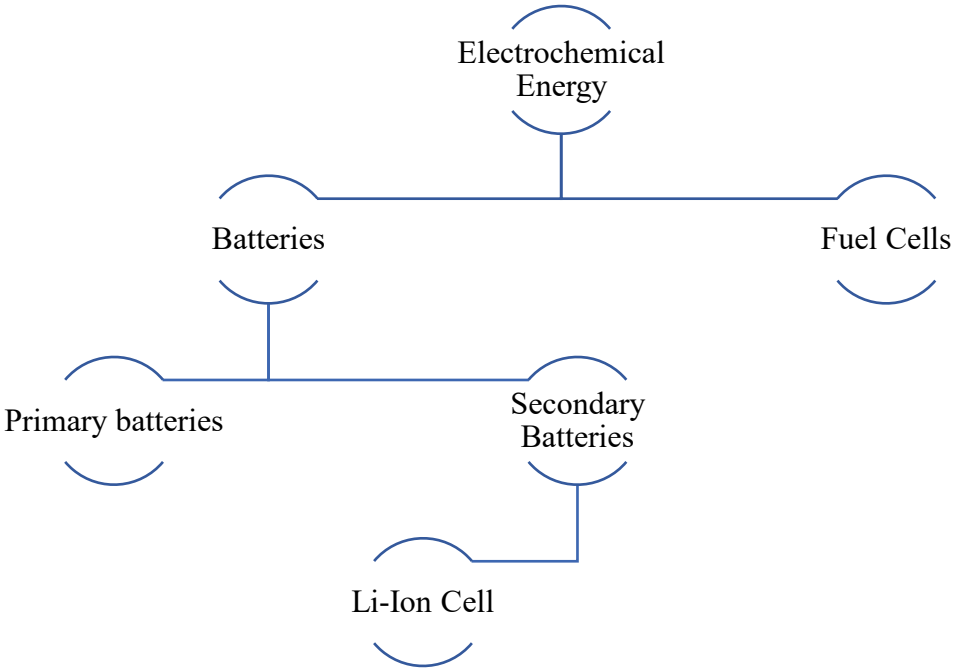

Figure 1: Classification of electrochemical energy

The Li-ion battery is a secondary battery with two electrodes and an electrolyte and with Li ions acting as the charge carriers. Intercalation is the working principle of Li-Ion batteries, it is a process where the Li^+ ions are repeatedly transported through the electrolyte and inserted or extracted from the electrode host structure depending on the oxidation or reduction reaction taking place at the electrode. One of the electrodes is graphite or lithium titanate ($Li_4Ti_5O_{12}$) *[8,9]*, the other electrode is usually one of the three materials: a layered oxide (such as lithium cobalt oxide), a polyanion (such as lithium iron phosphate), or a spinel (such as lithium manganese oxide). The electrolyte for the Li-ion battery is a lithium salt dissolved in a solvent. The salts that are commercially used in Li-ion batteries are lithium hexafluorophosphate (LiPF6), lithium-hexafluoro-arsenate-monohydrate (LiAsF6), lithium perchlorate (LiClO4), and lithium tetrafluoroborate (LiBF4) dissolved in organic solvents like ethylene carbonate (EC), diethyl carbonate (DEC) *[9]*. The arrangement of the Li-ion battery consists of a perforated separator, separating the anode and cathode to prevent the internal short circuiting of the battery, while allowing the charged ions to pass through it. During charging, the charge carriers move from the cathode through the electrolyte and are stored in the graphite anode. The more Li^+ ions are stored in the anode, the more electrical energy the battery delivers *[10]*. The cells reactions are *[9]*,

Cathode half-cell reaction: $LiMO_2 \rightleftharpoons Li_{1-x}MO_2 + xLi^+ + xe$

Anode half-cell reaction: $nC + xLi^+ + xe \rightleftharpoons Li_xC_n$

Full cell Reaction: $LiMO_2 + nC \rightleftharpoons Li_{1-x}MO_2 + Li_xC_n$

During charging in the cathode, the lithium present in the cathode material is oxidised by losing an electron and becoming positively charged Li^+ ions. These Li^+ ions travel through the electrolyte and are stored in the anode. During discharge, the Li^+ions are released from the anode, and they migrate back through the perforated separator to the cathode. The direction of the movement of the electrons dictates the direction of the current flowing in the circuit. The current flows in the opposite direction to the direction of the electrons in the outer circuit.

2.1Thermal runaway of Li-ion

Li-ion batteries are perfect candidates for energy storage owing to their energy and power densities. The energy of the batteries is a result of exothermic and gas-generating reactions *[11]*. The Li-ion battery is charged and discharged during its operation. During the initial charging cycles, the anode (graphite) of the Li-ion battery reacts with the electrolytic solution

and because of the reduction reactions of the electrolyte, a passive layer is formed on the electrode. The mechanism for the formation of the passive layer is not fully understood. The passive layer formed on the anode is called Solid Electrolyte Interphase (SEI) and enables the reversible charging and discharging of the batteries by preventing the exfoliation of the graphite electrode and the decomposition of the electrolyte *[12]*.

The SEI layer consists of stable and metastable compounds formed from the reduction reaction of the electrolyte. According to Yang et al. *[13],* the metastable compound present on the graphite electrode decomposes exothermically when the temperature of the battery increases to 85^{o}C and the graphite electrode is exposed without the passivation layer. This results in the formation of a secondary layer which decomposes simultaneously at 110^{o}C. The rapid increase in temperature can result in evaporation of the electrolyte at 140^{o}C and melting of the separator at 190^{o}C. Li-ion batteries contain both fuel and oxygen. Evaporation of the electrolyte can result in vigorous combustion if oxygen is present in the vicinity. Because of the spontaneous reactions occurring in the battery, the temperature increases drastically to 660^{o}C, where the aluminium can melt *[13]*. The temperature increase of one cell can transfer to the nearby cells and this situation can result in TR where the temperature of all the cells in the battery increases and this situation can result in an explosion of the battery module.

The temperature of the battery is determined by the amount of heat dissipated from the system. TR of the battery can be contained by finding the correct balance between the heat generated and the heat dissipated by the battery system. Achieving this balance is crucial because the exothermic reaction in the battery follows an exponential trend where the temperature increases rapidly, whereas the heat dissipation system follows a linear function. The amount of heat generated, if not contained, will result in TR of the system.

2.2 Thermal behavior of Li-ion cell

Heat in Li-ion cell is generated due to the chemical reaction taking place in the cell and the internal resistance of the cell. The heat generation varies during charging and discharging of the cell. Chakib Alaoui et al.,*[14]* explained that the heat absorption or release happens due to two different processes:

1. Heat generation during the chemical reaction
2. Heat generation due to internal resistance

2.2.1 Heat generation during the chemical reaction

Heat energy is dissipated or generated during the charging and discharging of the batteries. Thermodynamically, the heat released can be given as change in Gibb's free energy as,

$$\Delta G = \Delta H - T\Delta S$$

Where, ΔH is the enthalpy change of the chemical reaction and ΔS is the entropy change during the chemical reaction and ΔS can be expressed as *[15]*,

$$\Delta S = nF\frac{\delta E_{emf}}{\delta T}$$

Here, n is the charge number, F is the Faraday's constant and E_{emf} is the electromotive force of the cell. The entropy change corresponds to the heat absorbed or released during the reduction reaction or oxidation reaction in the electrode while charging or discharging the batteries. The total entropy of the system is the summation of the entropy change at anode and the entropy change at the cathode. Appropriate sign conventions are used for ΔS, positive (+) for exothermic and negative (–) for endothermic reactions taking place at the electrodes.

$$\Delta S = \Delta S_a + \Delta S_c$$

Here ΔS_a represents the entropy change at anode and ΔS_c represents the entropy change at the cathode. $T\Delta S$ is the thermal energy of the chemical reaction and it can be expressed as the reaction heat Q_r.

$$Q_r = T\Delta S$$

Therefore, the reaction heat Q_r can be expressed as,

$$Q_r = nFT(-\frac{\delta E_{emf}}{\delta T})$$

The reaction heat corresponds to heat released or absorbed during the intercalation of the Li-ions into the electrodes.

2.2.2 Heat generation due to internal resistance

E_{emf} of Li-ion batteries varies from the equilibrium value during the charging and discharging cycles owing to the electrochemical polarisation of the battery. During the polarisation process, work is done by the battery and therefore heat energy is generated. The heat energy released or absorbed due to the polarisation per unit time can be given by Q_r,

$$Q_r = I^2 R_p$$

R_p is the polarisation resistance developed during the polarisation process. Similarly, heat can be generated by the ohmic resistance of the battery per unit time. Internal Ohmic resistance (R_i) generates heat according to Joules Law and the heat is given by Q_j,

$$Q_j = I^2 R_i$$

The total heat generated by the battery during charge and discharge can be given by Q_{tc} and Q_{td} ,

$$Q_{tc} = -nFT\left(\frac{\delta E_{emf}}{\delta T}\right) + (R_{pc} + R_{ic})\, I^2$$

$$Q_{td} = -nFT\left(\frac{\delta E_{emf}}{\delta T}\right) + (R_{pd} + R_{id})\, I^2$$

During charging the current is lower and hence the reaction is endothermic which is the contrary during discharge. Depending on the charging and discharging rate, the cells fluctuate between endothermic and exothermic. According to Chakib Alaoui *[14]*, the reaction is endothermic at a rate of ≤ (C/5) and exothermic at a rate of ≥ (C/5).

3

Thermal Management of Li-ion batteries

The temperature increase owing to the internal resistance and the chemical reaction of the cell can result in an increase in temperature of the entire battery module. If the heat is not removed from the system, it can lead to TR of the Li-ion battery. In the worst case, bad thermal management can result in explosion of the vehicle. With increasing battery size and compact packing of the cells in the battery, Battery Thermal Management (BTM) becomes more critical, because the surface area available for heat extraction becomes less, resulting in lower heat transfer rate per unit rate of heat generation *[15]*. Much work is ongoing to find the right thermal management system for the individual types of Li-ion batteries. Each thermal management system has its own advantages and disadvantages, and one system cannot be used in all the situations. For efficient performance, the battery temperature should be kept between 15 and 35°C, so the cooling system should be perfectly designed for this. The cooling system should not be overdesigned (more than the required cooling) or under designed and many trade-offs like cost, weight of the system and power consumption has to be made.

BTM can be broadly classified into: 1. active BTM, and 2. passive BTM. The classification can be seen in Figure 2. Active cooling refers to systems that require power to function and the extra power source acts as the parasitic power decreasing the range of the vehicle. Passive systems are beneficial in terms of power consumption because they do not consume electricity. But the limitation is that we do not have control over the system. If the temperature rises drastically, passive cooling is ineffective. The different types of cooling systems are listed below, and the predominant systems are explained briefly.

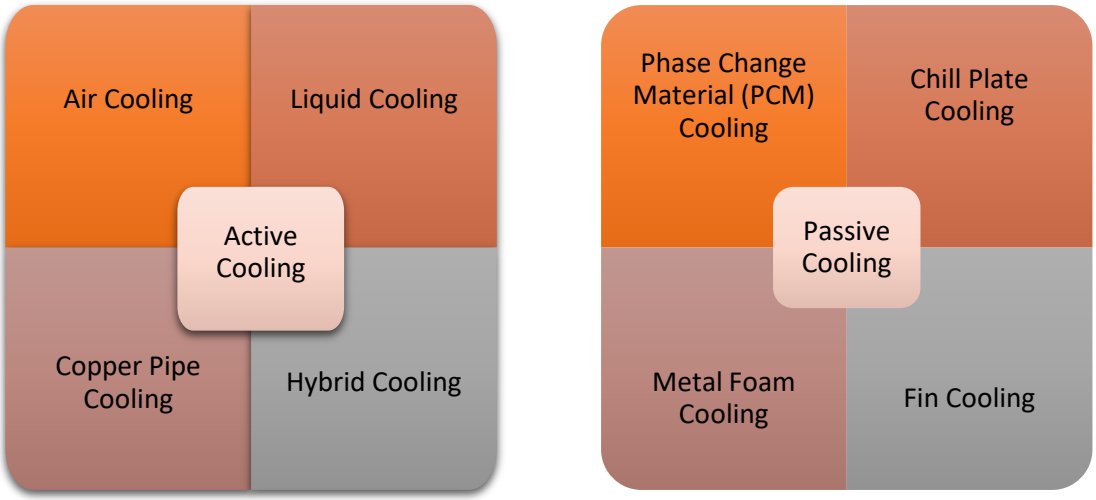

Figure 2: List of commercially available cooling systems available for LI-Ion batteries

3.1 Air Cooling

An air cooling system comprises of a cooling fan located in the battery module. Air from the cooling fan is forced through the gaps between the cells to remove the heat from the system. Wang et al. *[17,18]* studied the battery cooling system with the forced air cooling and different cell arrangements to circulate the air through the system and maintain the optimum working temperature for the battery. According to Wang et al. *[18]*, forced air cooling is effective for a temperature range between 20 and 35°C. If the temperature is beyond 35°C, higher flow speed is required, and higher parasitic energy is consumed by the cooling system. The other problems concerning the forced air cooling are,

- positioning of the fan in the battery module
- lower heat transfer coefficient compared to liquid and water
- obstructed path for the air flow
- temperature of the cooling air *[19]*

Among the above mentioned limitations, the major contributor is the fan positioning. If the cooling fan is placed at one end of the battery module, higher temperature is detected in the center of the battery pack owing to the mutual heating of the cells. If the fan is placed at the top of the battery pack, the farther ends of the module records higher temperature. The air cooling system is accountable for maintaining the optimal battery temperature, but when the cells reach a temperature of 40°C, the air cooling becomes ineffective and because of this limitation, forced air cooling is not suitable for thermal runaway situations.

3.2 Liquid Cooling

The heat transfer coefficient of a liquid is much larger than that of air, which makes the liquid cooling system better than the air-cooling system. The comparison of heat transfer coefficients of air, liquid and mineral oil can be seen in the Table 3*[20]*. The specific heat of water and mineral oil is larger than that of air, which makes the liquid transfer more heat and maintain the optimum temperature of the battery system and maintain temperature uniformity throughout the battery module. The efficiency of the system is outweighed by the complexity of the liquid cooling system. The liquid cooling system requires a pump to pump the coolant through the cells and transfer the heat from the battery pack to the coolant. The coolant reaches the heat exchanger, where the temperature of the coolant is transferred. The other disadvantages of the liquid cooling system are,

- Variation of coolant pressure
- Parasitic power to pump and heat exchanger
- Coolant transfer system

Variation of coolant pressure

The pump pumps the coolant into the battery module, when the pump malfunctions, the coolant pressure varies which disturbs the mass flow rate of the coolant. Decrease in the mas flow rate of the coolant reduces the amount of heat transfer. Decrease in the amount of heat transfer increases the temperature of the cell resulting in TR of the system.

Coolant transfer system

The coolant from the heat exchanger is pumped into the battery module and the coolant is either transferred through copper pipes or metal blocks as seen in Figure 3. The copper pipes increase the complexity of the design and the cost of the system is increased. The metal block increases the weight of the battery module and reduces the range of the vehicle.

S. No	Cooling Medium	Density	Specific Heat	Thermal Conductivity
1	Air	1.225	1006.43	0.0242
2	Water	1069	3323	0.3892
3	Mineral oil	924.1	1900	0.13

Table 3: Physical properties of different cooling mediums used in Li-ion cooling

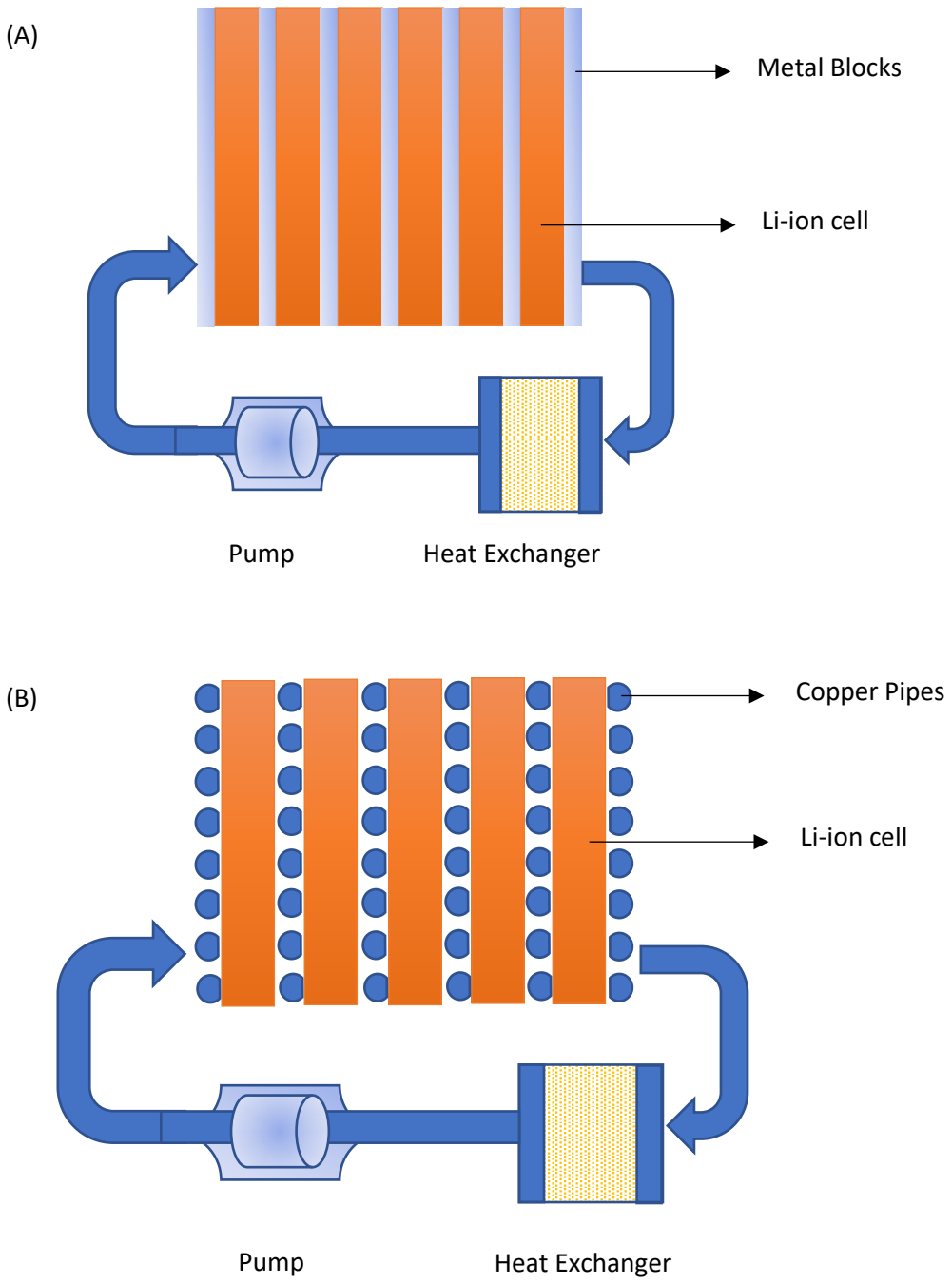

Figure 3: (A) Li-ion battery cooling with metal blocks; (B) Li-ion battery cooling system with copper pipes

3.3 Phase Change Material Cooling

The most popular method of BTM is phase change material (PCM) cooling. The PCM cooling uses paraffin wax to achieve a homogeneous temperature distribution, i.e. to reduce the excess heat generated by the cells during operation and regulate the temperature differences in the module. Paraffin wax has interesting physical properties some are contrasting to air and water used in the other cooling methods. The fusion point of the commercial paraffin wax (RT 44HC) is between 42.76ºC and 49.24ºC and the latent heat is 270 J/g *[21]*. RT 44HC has a

specific heat capacity of 2250 J. kg^{-1}. K^{-1} which is larger than the specific heat of air, and a thermal conductivity of 0.2 W. m^{-1}. K^{-1}, which is lower than that of water and mineral oil. Paraffin wax is chosen for PCM cooling depending on the latent heat of fusion, density of the wax and thermal conductivity. The organic PCM's that are commercially used in the market offer higher latent heat of fusion, constant phase change temperature over a specified range, and reliable chemical characteristics such as non-toxic, non-corrosive combined with an economic advantage of lower price *[22]*. Aggregate of all these makes PCM an interesting choice for thermal management of batteries. Li-ion batteries are cycled during their operation for several times and PCM has the advantage that it can retain the properties over different charging and discharging cycles. PCM cooling is a passive cooling system, and it is not dependent on other parts of the battery module like blowers, pumps, heat exchangers, fans, pipes, and other accessories.

3.3.1 Working of PCM

During the discharge cycle when the temperature of the cell is increasing, paraffin wax absorbs the latent heat released by conduction. The released heat energy is stored in the PCM, thus the excess heat from the Li-ion cells is removed and the battery temperature is reduced to a nominal working temperature. The heat energy stored in the PCM increases the temperature of the PCM and it undergoes a phase change from solid to liquid isothermally *[23]*. During cooling, the stored latent heat is released through a natural convection process due to the buoyancy of the liquid and the liquid wax undergoes a phase transformation into the solid state. Thus, PCM cooling absorbs and stores heat depending on the required thermal load. PCM dissipates excess by conduction and convection and the heat dissipation characteristics of PCM is greater than the heat dissipation of air cooling by convection *[23]*.

3.4 Hybrid PCM

PCM cooling has advantages over the air-cooling due to its better heat transfer characteristics but is inferior when compared to liquid cooling systems. The liquid cooling systems has higher heat transfer rates due to the higher thermal conductivity of the liquid over the PCM. This conflict can be resolved by increasing the thermal conductivity of the PCM material. The thermal conductivity can be increased by adding other materials with higher conductivity than wax. The popular materials that are added to create a composite PCM are aluminium, copper, and graphite. These additives increase the conductivity and the heat from the cells is dissipated fast and can speed up the melting of wax *[22]*.

4

Cooling Method

The Li-ion batteries used for the current study is a rectangular type of battery of dimensions 236(length)*115(height) mm with a gap of 3mm between two cells. The cells are held in place with the help of the push pads at the ends and a cooling plate at the bottom of the module (see Figure 4.).

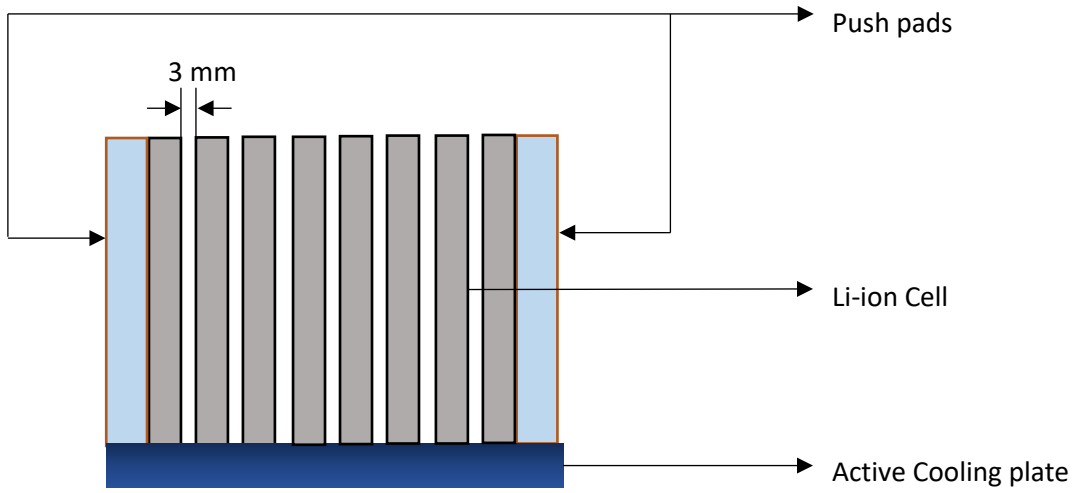

Figure 4: Arrangement of different components in a Li-ion battery

The space available between each cell is 3 mm. A thermal pad is placed between the two cells for two different functions,

- Thermal function
- Mechanical function.

4.1 Thermal Function

Li-ion cells produce heat energy as a by-product of the chemical reactions taking place in the cells. The heat from one cell should not transfer to the neighboring cell, the padding is a ceramic pad of 3mm in thickness.

4.2 Mechanical Function

Intercalation of the electrodes in Li-ion batteries induces volume changes in the active materials of the cell. Volume changes in the active materials in addition to the gasses emitted

during the chemical reaction create a stress on the walls of the aluminium cell cans. When the compressive stress exceeds the tensile stress of the cans, the aluminium can bulges causing the cans to swell. The swelling profile of the cans can be seen in Figure 5.

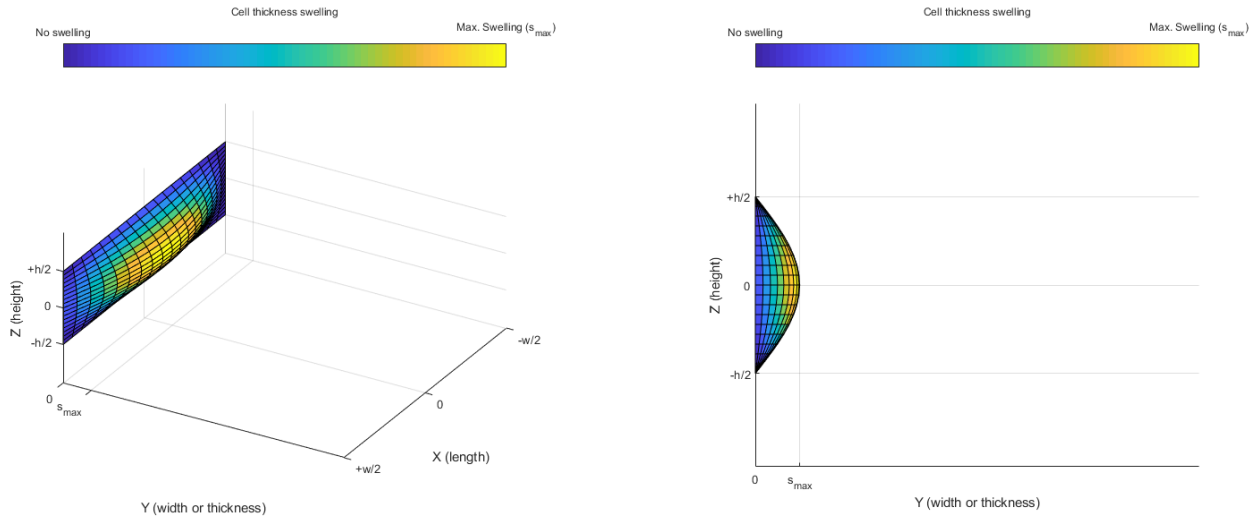

Figure 5: Swelling Profile of Aluminium cans used for holding the electrolyte and the electrodes

The maximum swelling was measured to be 1.8 mm for a force of 25kN. From this, we can measure the strain on the aluminium cell cans.

Force during swelling: 25KN

Area considered: 10 x10 cm^2

Youngs Modulus of aluminium = 69 GPa

Thickness of the aluminium can = 0.7 mm

$$\text{Stress } = \frac{25 * 10^3}{10 * 10 * 10^{-4}} = 2.5 * 10^6\ Pa = \mathbf{2.5\ MPa}$$

$$Strain = \frac{Stress}{Young's\ Modulus}$$

$$Strain = \frac{2.5 * 10^6}{69 * 10^9} = 0.036 * 10^{-3} = \mathbf{36.23 * 10^{-6}}$$

$$Strain = \frac{\Delta l}{Length}$$

$$\Delta l = Strain * Length = 36.23 * 10^{-6} * 0.7 * 10^{-3} = \mathbf{25.361 * 10^{-9} m}$$

The strain on the aluminium cells is 25.361 nm which is small. The strain from the above calculation is calculated considering a non-cyclic loading. The Li-ion cells expands and contracts during the operation resulting in a fatigue loading on the cell cans. In fatigue loading, the strain is accumulated on each cycle of the loading. The progressive localised strain adds up and the summation of the strain crosses the yield limit of the aluminium cans resulting in a plastic deformation of the material.

The cooling mechanism should consider both the mechanical and the thermal aspect as discussed above. The cooling methods that are commercially available in the market require space between the cells to extract the heat generated by the cells. Air cooling and direct liquid cooling systems require the fluid to absorb the heat around the cells and to return to the heat exchanger for reducing the temperature of the fluid. Since, the space available around the cells is 3 mm, much fluid cannot flow through. The limitations also come with the need for other external elements like pump, heat exchanger, a leak proof design suitable to hold the fluid, the parasitic power of the accessories, etc. PCM systems do not have stringent requirements like the air- and water-cooling systems but the limitation comes with the amount of wax available to cool the cells. According to Giuliano et al. *[23]*, the volume of the paraffin wax available is directly proportional to the cooling achieved. If the amount of wax is reduced, the effectiveness of the PCM is reduced. So, PCM cooling is not a suitable cooling method for this setup. Fin cooling is an effective way, but it increases the weight of the system by 40% *[2]*.

The cooling system should not require more space and it should function well in thermal and mechanical situations. The system in consideration is an indirect liquid cooling method. The heat from the cells is prevented from transferring to the neighboring cells by providing a thermal insulation between the cells. The thermal insulation provides a thermal gradient path such that the heat is not allowed to transfer through the walls of the aluminum cell. Instead, the heat is removed at the bottom through a cooling plate with circulating water and glycol in the plate. The thermal insulation is provided by a TBC. The heat flow direction can be illustrated in analogy with an electrical circuit. The heat flow resembles the electrons in an electrical circuit, the electrons travel in the direction with the least resistance, similarly the heat transport in a path with least thermal resistance. The TBC provides the thermal resistance as the conductivity is low compared to the thick aluminum block with cooling channels.

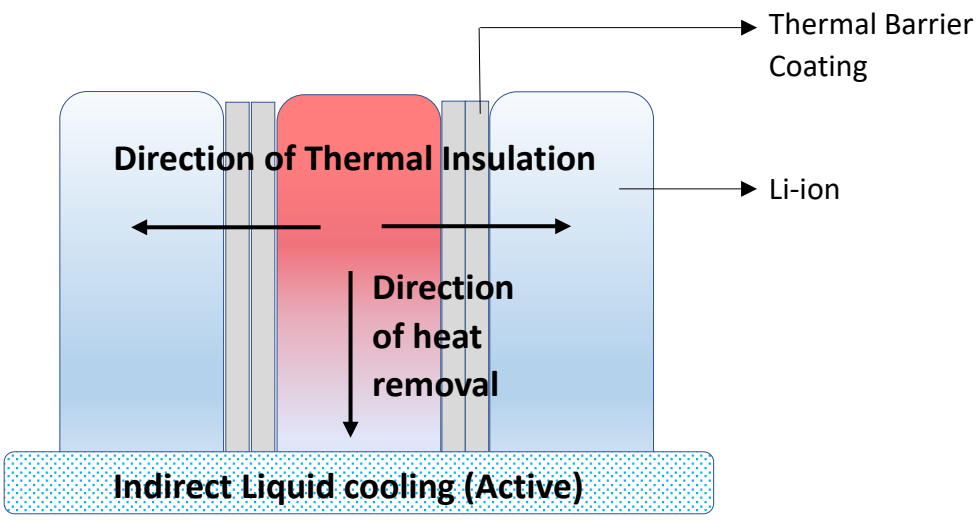

Figure 6: Direction of thermal insulation and heat removal in Li-ion batteries

5

Thermal Barrier Coating

The purpose of a TBC is to provide a thermal protection to the material that is underneath the coating and to increase the lifetime of the material *[24]*. The TBC should be actively cooled to remove the heat from the system. The typical properties of the TBC are low thermal conductivity, no undesirable phase transformation at the operating temperatures, high thermal stability, high melting point, corrosion resistant, etc., The TBC is typically a multi-layered coating consisting of a bond coat, a thermally grown oxide layer, and a top coat over the metallic substrate to be protected as seen in Figure 7.

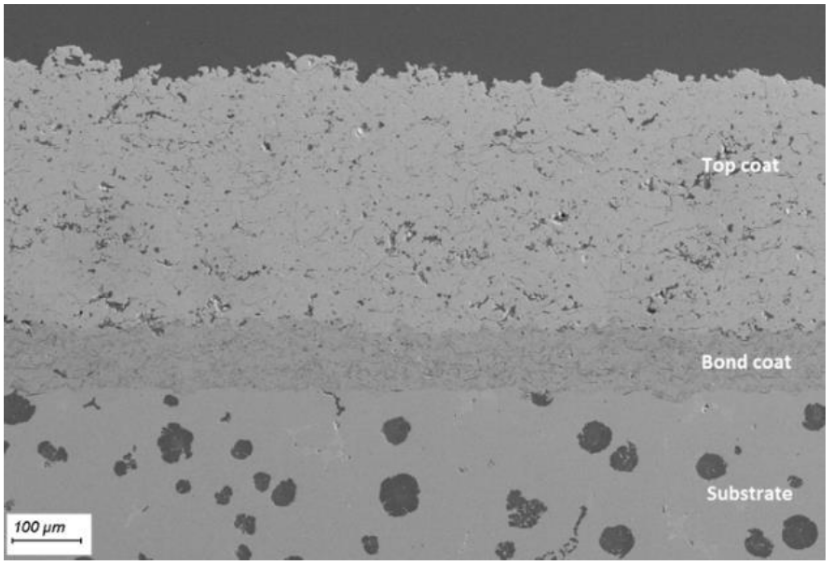

Figure 7: Microstructure of TBC with top coat, bond coat and substrate illustrated

P.C: Anders Thibblin Doctoral dissertation, KTH, Royal Institute of Technology [26]

5.1 Bond Coat

Each layer has an intended role; the primary role of the bond coat is to provide bonding between the substrate and the top coat. The bond coat is an alloy of type MCrAlX where M represents the metal which can be Ni, Co or Fe. The X represents the oxygen active elements like Ti, Zr, Hf, Si *[25]*. The other roles of the bond coat are to provide a ductile layer to prevent

the crack propagation to the top coat *[26]*. The metallic bond coat layer is supposed to match the coefficient of thermal expansion of the substrate and the ceramic top coat.

5.2 Top Coat

The top coat is a ceramic layer coated to provide a thermal insulation to the other coating layers and the substrate. The top coat can be a single layer or a combination of layers to attain the required thermal and mechanical properties. The monolayer coating consists of one type of ceramic material coated on the bond coat. The multilayer coating consists of different materials or different types of microstructures coated on the bond coat material. The types of top coat material are explained below,

5.2.1 Monolayer Coating -Yttria Stabilised Zirconia

Yttria stabilised zirconia (YSZ) is the most used thermal barrier coating because of its unique properties such as low thermal conductivity of 2 $W/m.K$ and its high coefficient of thermal expansion (CTE) of $8.9\ to\ 10.6 * 10^{-6}K^{-1}$ when compared to other ceramics *[29]*. In addition to these, YSZ has the capability to inhibit the crack propagation by transformation toughening *[27],[28]*. Transformation toughening is a phenomenon in which the material around the crack changes from a tetragonal to a monoclinic crystal structure due to the stress created by the growing crack. This transformation leads to a 4% increase in volume, thus enhancing the fracture toughness of the material *[29]*.

YSZ layers can be produced by different thermal spray processes such as Atmospheric Plasma Spraying, Suspension Plasma Spraying, High Velocity Oxy Fuel and the properties of the coating can be tweaked by changing the microstructure to achieve the desirable properties. According to Li et al.,[21] YSZ coatings produced by plasma spraying with large segmentation cracks, have better strain tolerance. Segmentation coatings can be produced during hot spraying conditions. The segmented coatings have lower porosity and higher lamellar bonding which in turn has better mechanical properties attributed by the microstructure. The fracture toughness increases from $1.7 - 2.0\ MPa\sqrt{m}$ to $2.0 - 2.3\ MPa\sqrt{m}$ *[5]*.

5.2.2 Multilayer Coating

Multilayer coating consists of repetition of two layers coated by using various techniques like diffusion bonding, EB-PVD, APS. The layers can be ceramic/ceramic, ceramic/metal, ceramic/polymer depending on the properties required. Multi-layer coatings have better resistance to fracture compared to monolayer coatings *[27]*. The properties of the coating

depend on the properties of the individual layer, number of layers and thickness of each layer. Increasing the number of layers increases the interface between each layer. Increase in the number of interfaces, increases the effective barrier for crack propagation *[27], [28].* The cell expands during its lifetime and during the expansion, there will be a tensile stress on the coating from the inside of the cell. Ceramic materials are not performing well under tensile loading conditions. The crack growth can be controlled by maximising the critical stress intensity required for crack propagation by including a ductile phase which remains intact, bridging the crack faces, in the wake of a growing crack *[28].* Presence of a ductile layer in between the ceramic layers increases the toughness of the coating by accommodating the plastic strain *[27].* When a crack propagates in the ceramic layer and reaches the metallic ductile layer, it activates the slip mechanism in the metal where a part of the fracture energy gets dissipated, and a new crack is nucleated in the hard ceramic layer to propagate further. For higher loads, the fracture of the ceramic layers is catastrophic, and the metallic layers are plastically deformed in the form of rotation, sliding, and twinning of the grains *[27], [28].*

6

Coating Method

Zirconia based ceramic material can be coated with methods that can produce higher energies to melt, evaporate or chemically fragment the ceramic material and deposit them on the substrate. Higher energies required for melting the ceramic can be produced by various methods like plasma spraying, High Velocity Oxygen Fuel (HVOF), detonation and one of the popular methods is plasma spraying *[24]*. The plasma spraying can be classified into Atmospheric Plasma Spraying (APS) or Suspension Plasma Spraying (SPS) based on the form of raw material used for coating.

6.1 APS

APS is a versatile thermal coating technique with a wide variety of coating materials that can be used. In APS, an electric arc is initiated between the tungsten cathode and water-cooled copper anode. The arc dissociates the gas, and the gas molecules are ionized. The electrons are taken to an excited state of energy. When the electrons return to a lower energy state, energy is released, creating a plasma. The plasma is accelerated towards the substrate with high pressure. The temperature of the plasma jet ranges from 500ºC to 25000ºC with a velocity of 80 to 300m/s *[24]*. The coating material in the form of powder is injected into the plasma. The plasma with high pressure and temperature melts the powder particles and carries the molten powder to the surface of the substrate material. On collision with the substrate, the molten particles flattens and solidifies immediately called as splats (seen in Figure 8). Deposition of splats over one another creates a lamellar structure perpendicular to the direction of the substrate*[26]*. The obtained coating is porous in nature and the porosity can be controlled by changing the process parameters like type of carrier gas used, velocity of the gas, cooling of the substrate, nozzle diameter, powder size, feed rate, voltage between the electrodes. A visual representation of the APS system can be seen in Figure 9. The top coat used in this study is YSZ (5% Yttria stabilisation) mixed with a polymer to increase the porosity of the coating up to 40%. Increase in porosity decreases the thermal conductivity of the coating *[32]*. The ceramic material is coated on a plate of 100 X 100 mm plate of thickness 3mm.

Figure 8: Splats formed on the substrate during APS Coating

P.C: Anders Thibblin Doctoral dissertation, KTH, Royal Institute of Technology [26]

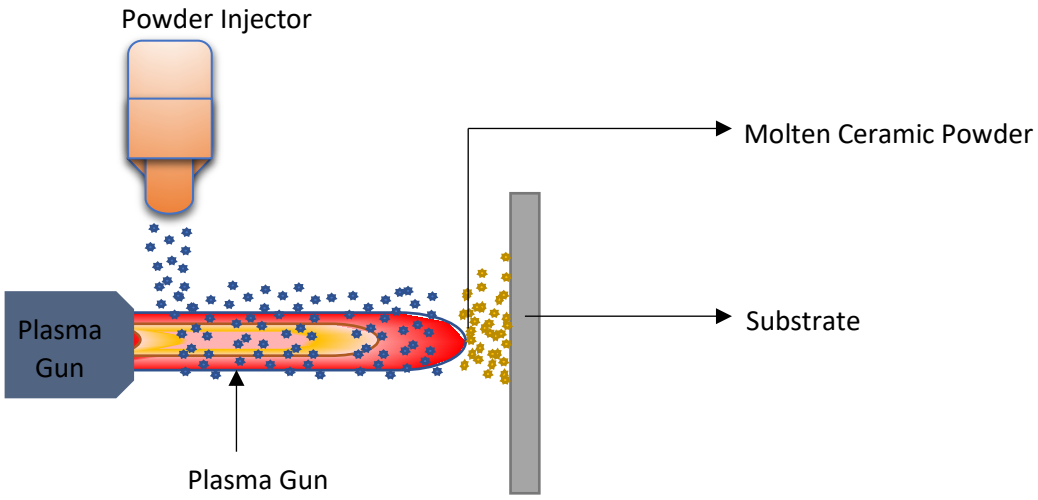

Figure 9: Visual representation of APS

6.2 SPS

SPS has benefits over the APS process where particles of smaller size can be used for coating. The ceramic particles to be coated are suspended in a liquid and the suspended liquid is sprayed on the substrate. The principle of working is the same as the APS with a change in the type of raw material used. The suspended ceramic particles are fed into the plasma, the plasma atomises the suspension and the liquid used for suspension is evaporated and the ceramic particles are melted and carried to the substrate. The microstructure of the coating can be varied

by changing the parameters of the coating process. The different microstructures that can be achieved in SPS process are lamellar, columnar, and vertically cracked structures *[31]*. Thermal conductivity of the coating can be varied by varying the porosity of the coating microstructure, a thermal conductivity of 0.5 to 0.9 $Wm^{-1}K^{-1}$can be achieved in SPS *[32]*. The top coat used for the study is YSZ with 5% yttria.

7

Experiments

The coating system used to prevent the thermal propagation in Li-ion batteries should be tested for mechanical and thermal properties as discussed in section 4.

7.1 Thermal testing

The thermal testing planned for testing the system heats the substrate from one direction and the heat transfer is measured on the other side of the sample. When the specimen is heated, the thermal energy can be dissipated in all the three directions and the conductive heat transfer through a material in 3 dimensions can be represented by the following equation,

$$\frac{\partial(\mathrm{i}Q_x + \mathrm{j}Q_y + \mathrm{k}Q_z)}{\partial \mathrm{t}} = -KA(\left(\frac{i\,\partial \mathrm{T}}{\partial \mathrm{x}}\right) + \left(\frac{j\,\partial \mathrm{T}}{\partial \mathrm{y}}\right) + \left(\frac{k\,\partial \mathrm{T}}{\partial \mathrm{z}}\right))$$

Measuring the heat transfer in all the three directions is critical and therefore the setup is designed to measure the heat transfer in one direction by insulating the transfer of heat in other directions. One dimensional thermal conductivity can be given by,

$$\frac{\mathrm{dQ}}{\mathrm{dt}} = -KA\left(\frac{\mathrm{dT}}{\mathrm{dx}}\right)$$

Here Q is the heat flux through the system, K is the thermal conductivity of the sample, $\frac{\mathrm{dT}}{\mathrm{dx}}$ is the local temperature gradient. The setup consists of a heating element insulated inside a thermal insulating material PEEK (seen in Figure 11) and a thermocouple (number 1) is positioned on top of the heating element to measure the temperature increase. The substrate material with the coating is placed on top of the heating element (seen in Figure 12). The temperature on the coating is measured using a thermocouple (number 2) and a heavy block of copper is placed on top of the coated material from which the temperature is measured. A layer of thermal paste is applied on the thermocouple in between the heating element and the sample, also, in between the Physical representation of the system is seen in Figure10. The thermocouples were connected to the thermocouple calibrators to measure the temperature. The temperature measurements were taken at an interval of 30 seconds. The setup measures

the thermal conductivity based on the non-steady state measurement technique which records the heat change during the heating process *[33]*.

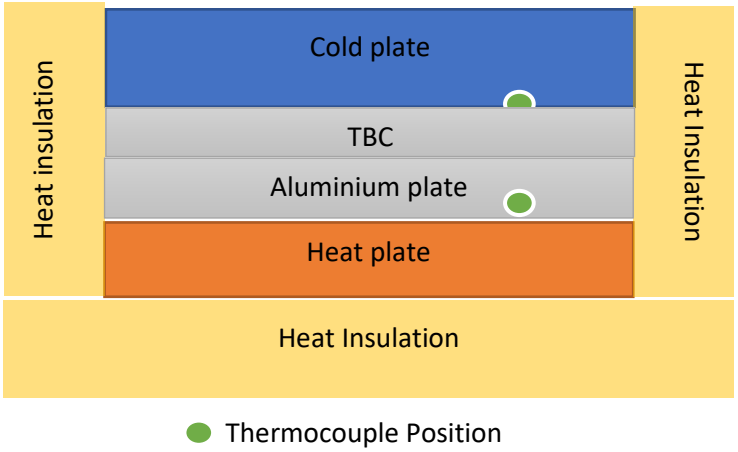

Figure 10: Visual representation of thermal test setup

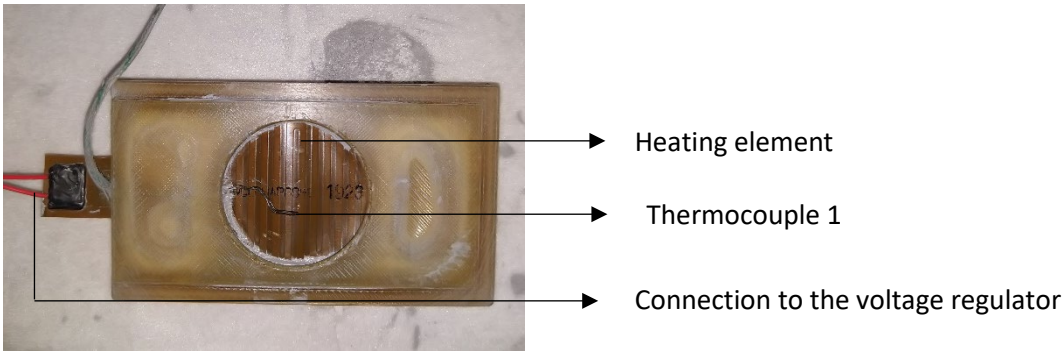

Figure 11: Thermal testing setup showing the heating element

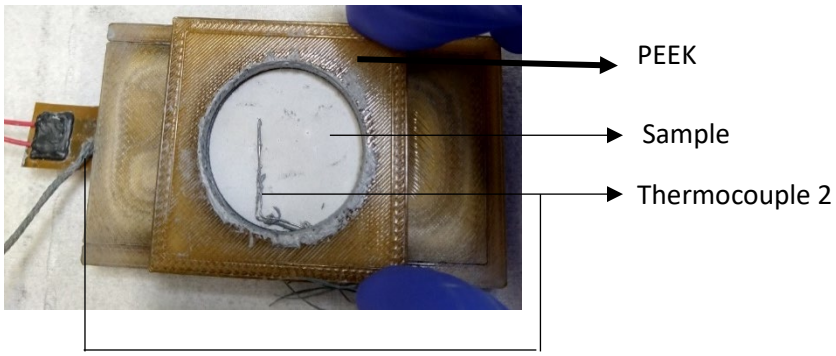

Figure 12: Sample placed on the heating element

7.1.1 Sample Preparation

The sample for the thermal testing is prepared by cutting the coated plates of 100 X 100 X 3 mm to 30mm coins by water jet cutting (seen in Figure 13). The coins were cleaned in an ultrasonic cleaning machine for 10 minutes to remove dirt or grease if present on the material. The cleaned sample is grinded in the corners to avoid sharp edges.

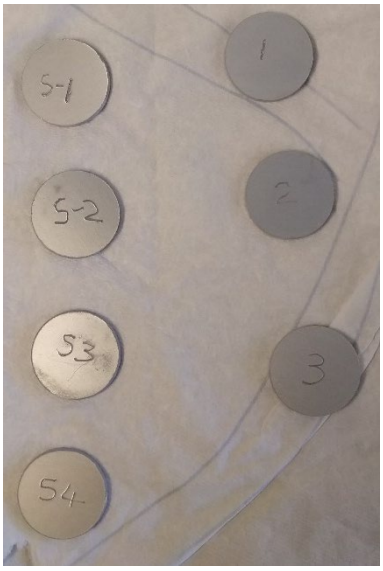

Figure 13: Coin Samples used for thermal testing

7.2 Mechanical Testing

7.2.1 Drop Weight Test

To understand the crack propagation in the coatings, impact testing is performed on the sample using drop weight test method (schematic representation is see in Figure 13). A load of 1000g± 10g is dropped on the aluminum side with the coating facing downwards. Indents were made with different forces on the sample by changing the height from which the load is dropped. The load was dropped from heights varying from 20 cm to 100 cm. The coated sample with indents for varying load is seen in Figure 14.

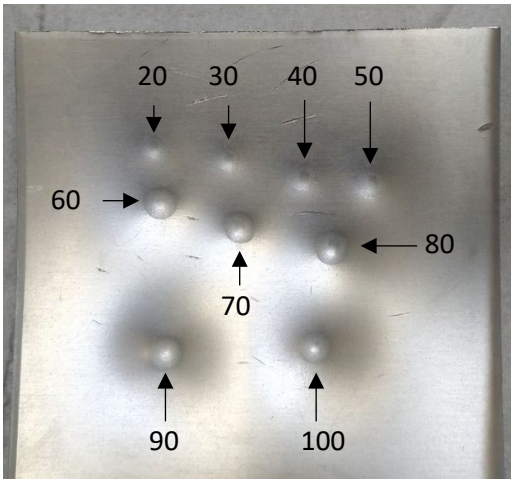

Figure 14: Position of indents corresponding to different drop heights

7.2.2 Bending testing

Li-ion cells expand and contract during the operation. The expansion profile can be seen in Figure 5. To simulate the expansion of the cell, the maximum expansion of the cell is measured, and an indenter is designed specifically to match the dimensions of the swelling of the aluminium can. The indenter is loaded in a universal tensile testing machine and the sample is loaded repeatedly for a maximum force of 25 kN.

8

Characterization

8.1 SEM

The coin samples used for the thermal testing are cleaned with ultrasonic cleaning to remove the thermal paste from the surface of the coating. The coin samples are cut into semi circles to measure the coating thickness of the coins in the SEM. The coins were mounted by hot mounting using thermo setting resin. The mounted samples are cleaned in an ultrasonic machine. The cleaned samples were loaded inside the vacuum chamber of the Zeiss SEM. Once the vacuum is reached, a voltage of 15 to 17 kV was used to focus the electron beam on the sample. Secondary electrons were used to determine the coating thickness of the samples and EDX is used for elemental analysis.

8.2 Stereo Microscope

Stereo Microscope Zeiss Discovery V12 was used for studying the cracked samples from drop weight test. The samples from the drop weight test are examined under the stereo microscope for understanding the crack propagation in the two different types of coatings.

9

Results and Discussion

9.1 Thermal Testing

Thermal conductivity of a material depends on the porosity of the material *[35]*. The coating used for testing has varying porosity across the cross section of the sample and to compare with two different coatings, rather than measuring the thermal conductivity of the sample, the following parameter is measured and reported.

$$\frac{dQ}{-KA} = \left(\frac{dT}{dx}\right)$$

The local temperature gradient can help us visualize the material's ability to transfer the heat from one side to the other. The aluminum coin sample with the coating is heated from one side and the temperature is measured on coating side. The heating element is heated at three different heating rates corresponding to 8V, 12V, 16V. Initially, aluminum coins were used to determine the maximum temperature that can be reached for the corresponding voltage. Figure 15 shows the time taken to reach the maximum temperature corresponding to the applied voltage and the time taken to reach the temperature. The peak temperature was set to 120°C to

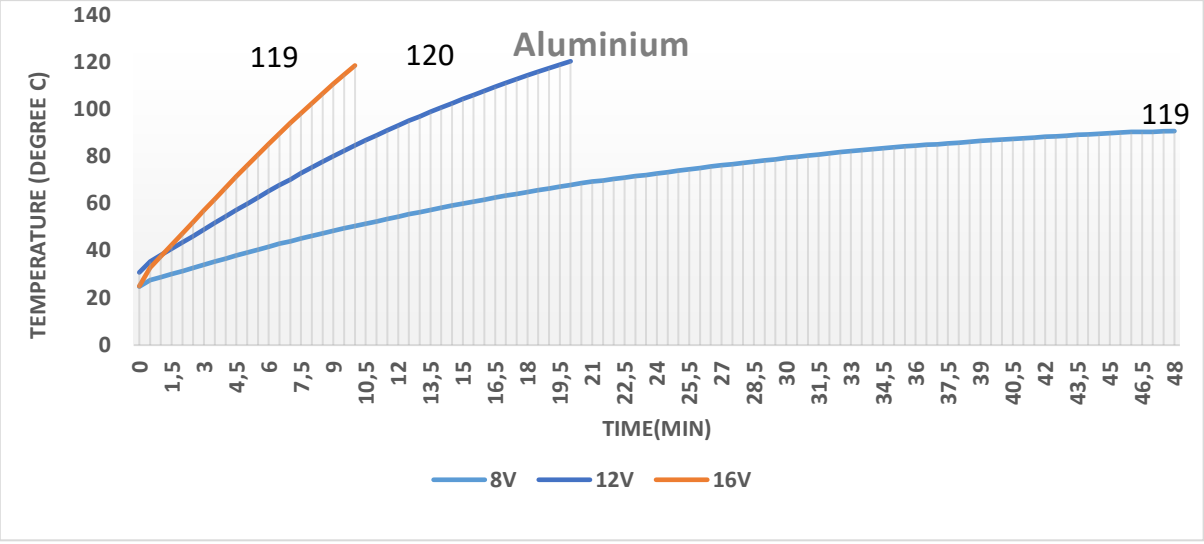

Figure 15: Time taken for reaching 120°C for the corresponding voltage

remain within the peak working temperature of PEEK and this temperature was reached in 10 minutes and longer time was taken for lower voltages.

A graph for local temperature gradient vs time was plotted for aluminum coin sample and is considered as the reference (seen in Figure 16). From the graph we can see that for a higher heating rate, the temperature reached on the surface of the coin sample is not uniform. For 16V the gradient is increasing steeply with time which denotes that a steady state is not reached within the coin. And for a voltage of 12V and 8V, a constant heating of the coin sample is seen. Therefore, for testing the samples, 10V is used.

The same experiment was repeated for aluminum coins with YSZ coated by APS and SPS and the results were plotted in the form of graphs (seen in Figure 17 and Figure 18).

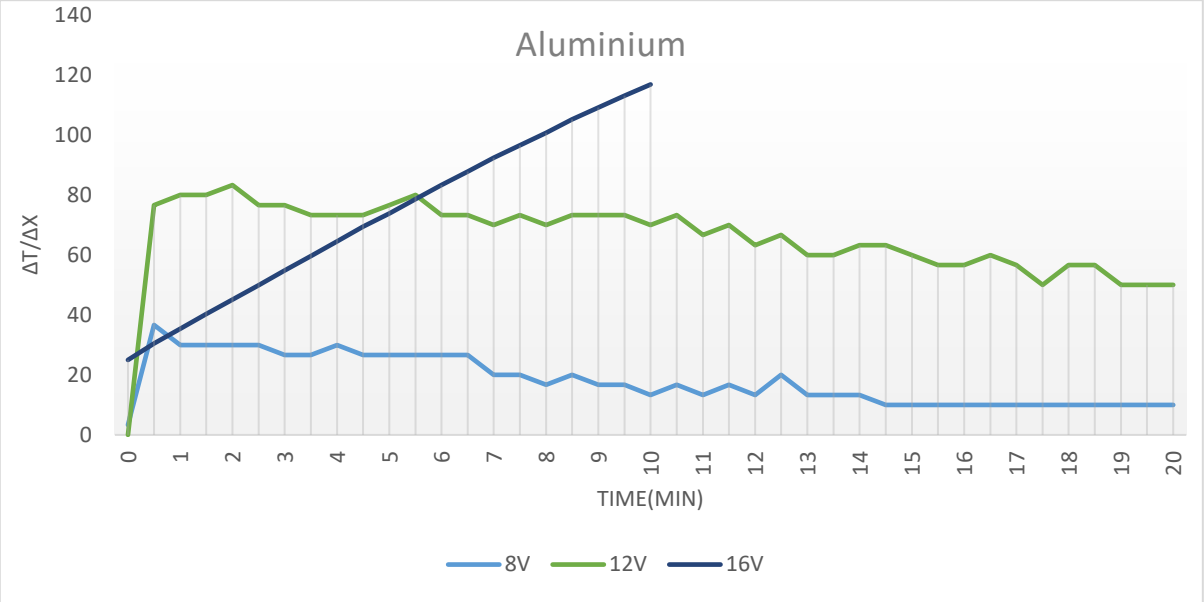

Figure 16: Local temperature gradient vs time for aluminum coin sample

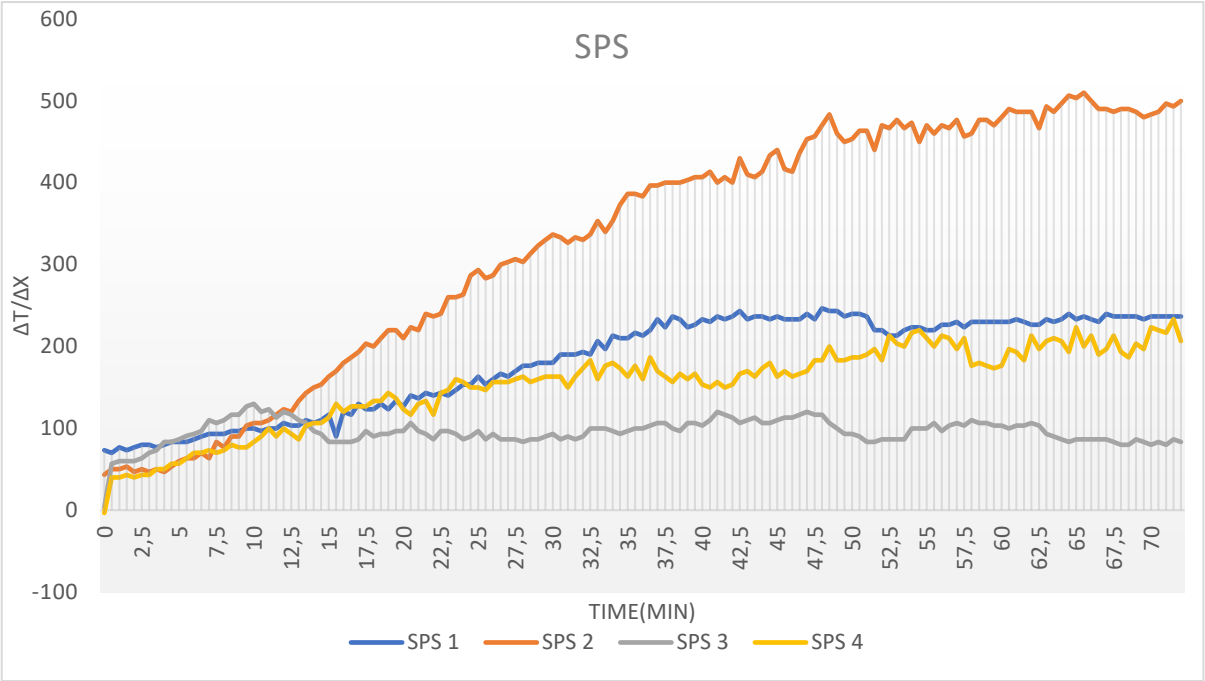

Figure 17: Local temperature gradient vs time for SPS coating

The coin samples SPS1 and SPS2 were taken from one plate and the samples SPS3, SPS4 were taken from another plate. Similarly, APS1 and APS2 were taken from one plate and APS 3 is taken from a different plate. The trend of variation of the local temperature gradient for all the samples was expected to be similar but huge variations are seen on the coins taken from the same plate. Table 4 shows the local temperature gradient for SPS1, SPS2, SPS3, SPS4 after 34 minutes. It can be seen that SPS 2 has a better temperature gradient which signifies that the temperature on the aluminium side and the coating side of the coin is varying by a greater margin. This represents that SPS 2 is having a better thermal resistivity. Theoretically, coins

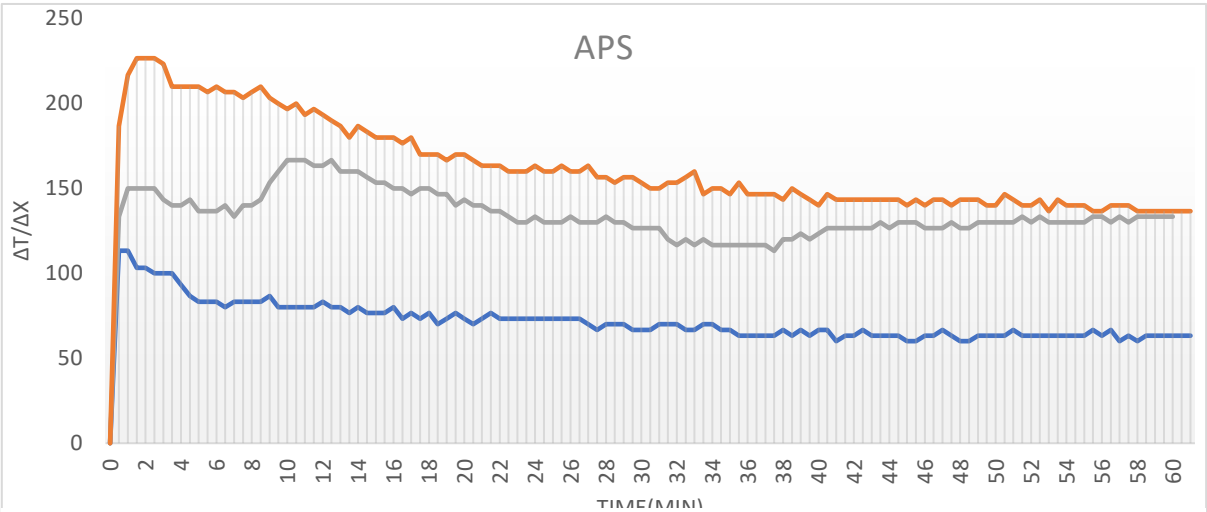

Figure 18: Local temperature gradient vs time for APS

taken from the same plate should have a similar thermal resistivity as the coating is uniform across a single plate. The difference can be because of two reasons; 1) Thermal bridges, 2) Different coating thickness across the plate. The greater margin of thermal resistivity across the plate shows that the heat is dissipated in other directions through thermal bridges.

Table 4: Local temperature gradient for SPS1, SPS2, SPS3, SPS4 after 34 minutes

Time (Min)	SPS 1	SPS 2	SPS 3	SPS 4
34	196.6667	340	100	176.6667

The thermal paste having a higher thermal conductivity can act as a thermal bridge if the thermal paste is applied on the sample as seen in Figure 19. The thermal paste can occupy the outer surface area of the coin and the heat from the heating element rather than passing through the coin, it can choose a least resistant path around the sample through the thermal paste.

Figure 19: Improper application of thermal paste

The possibility of heat transferring through the thermal paste is avoided by applying a minimum amount of paste on the thermocouples, so the paste does not reach the curved surface of the coin. The coins are cut into half to determine the coating thickness in SEM. The SEM images for the different coatings are seen in Figure 20 to Figure 23. SPS2 sample has an average coating thickness of 270 µm whereas SPS3 has a coating thickness of 80 µm. The variation of the coating thickness is reflected in the thermal testing. We can see that SPS2 has better thermal resistivity than SPS3 which is seen in Figure 17. The surface of the substrate is uneven, as seen in Figure 22. The unevenness of the substrate leads to improper bond coat on the substrate. The SPS coating has detached from the substrate and the detachment is because of the improper

bonding between the substrate and the coating. A similar trend is uneven coating and can be seen in APS coating. APS1 coating has a coating thickness of 249.2 µm whereas APS3 has a coating thickness of 323.2 µm. The difference in coating thickness has its impact on the thermal performance of the coating, which is seen in Figure 18, where APS3 has better thermal resistivity when compared to APS1.

Figure 2014: SEM image showing SPS coating on aluminum substrate of sample SPS2

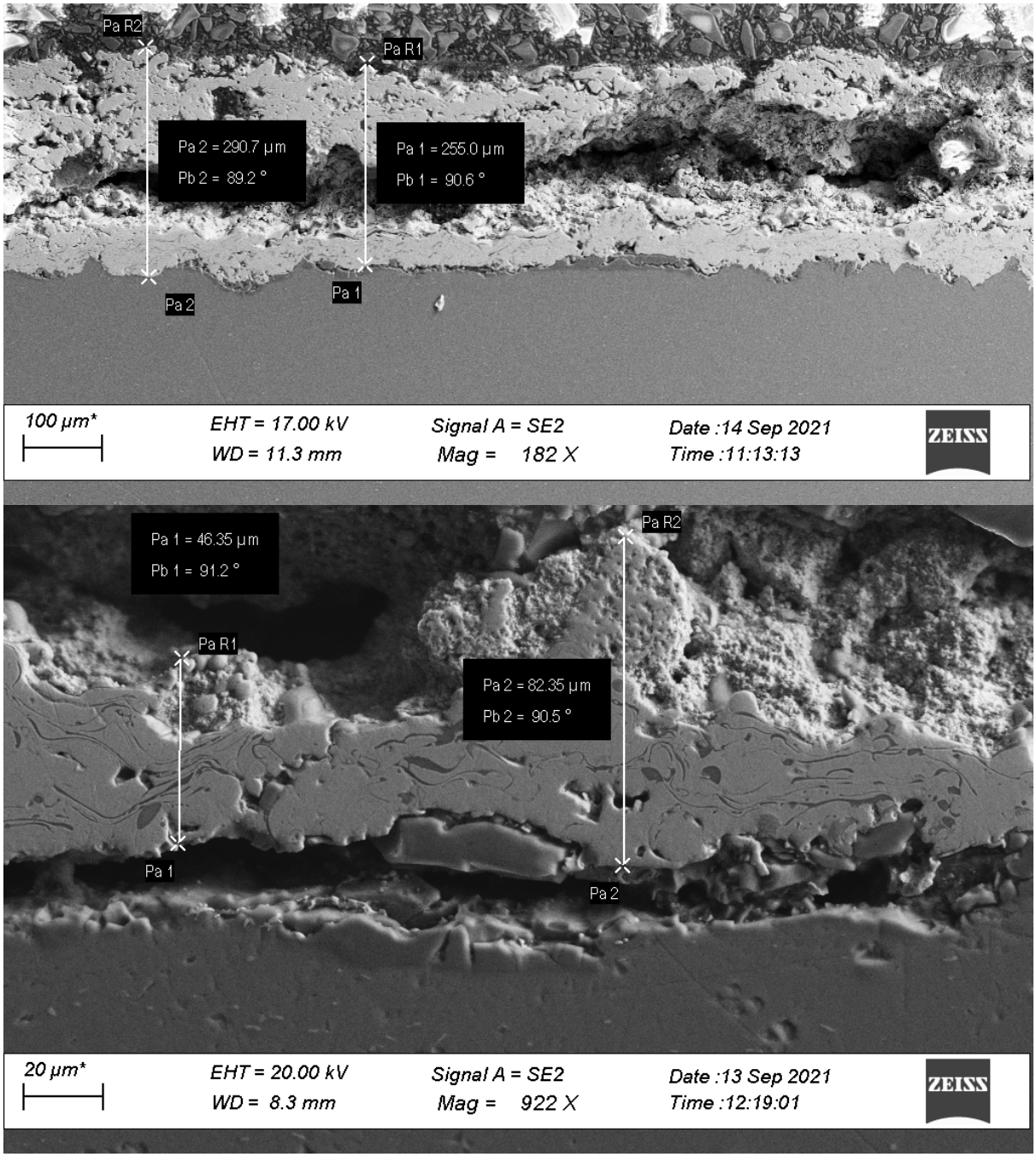

Figure 21: SEM image showing SPS coating on aluminum substrate of sample SPS3

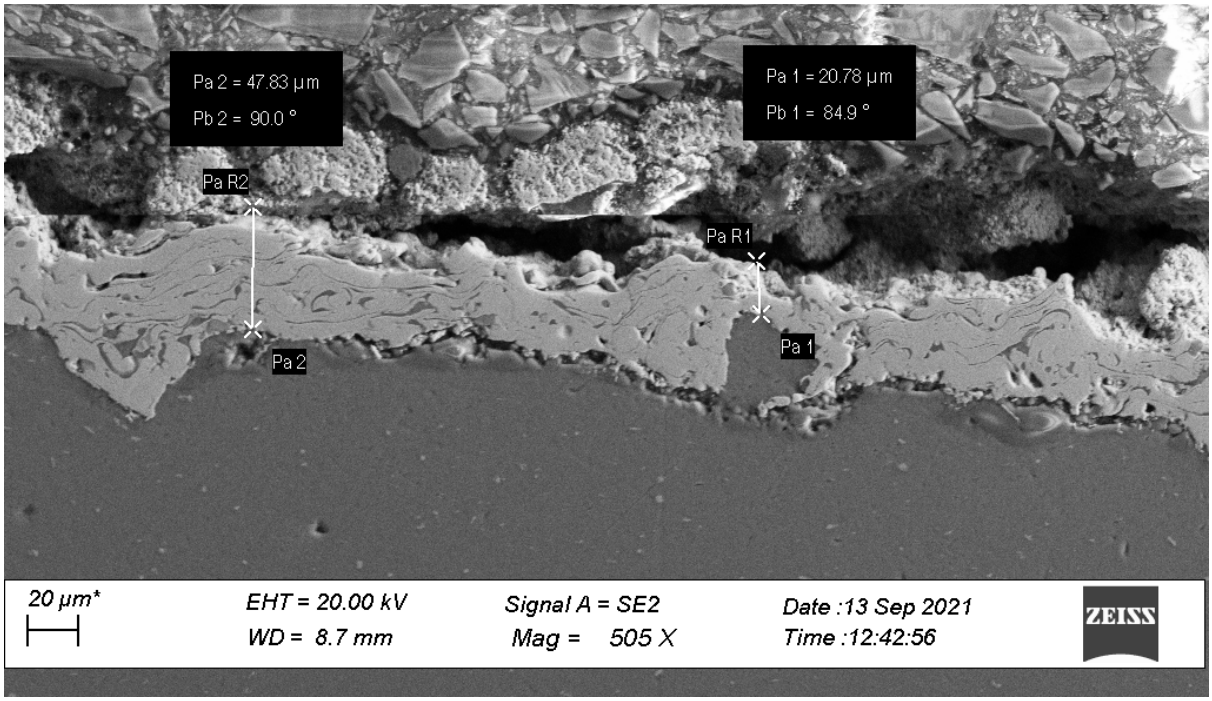

Figure 22: SEM image showing the bond coat in SPS coating

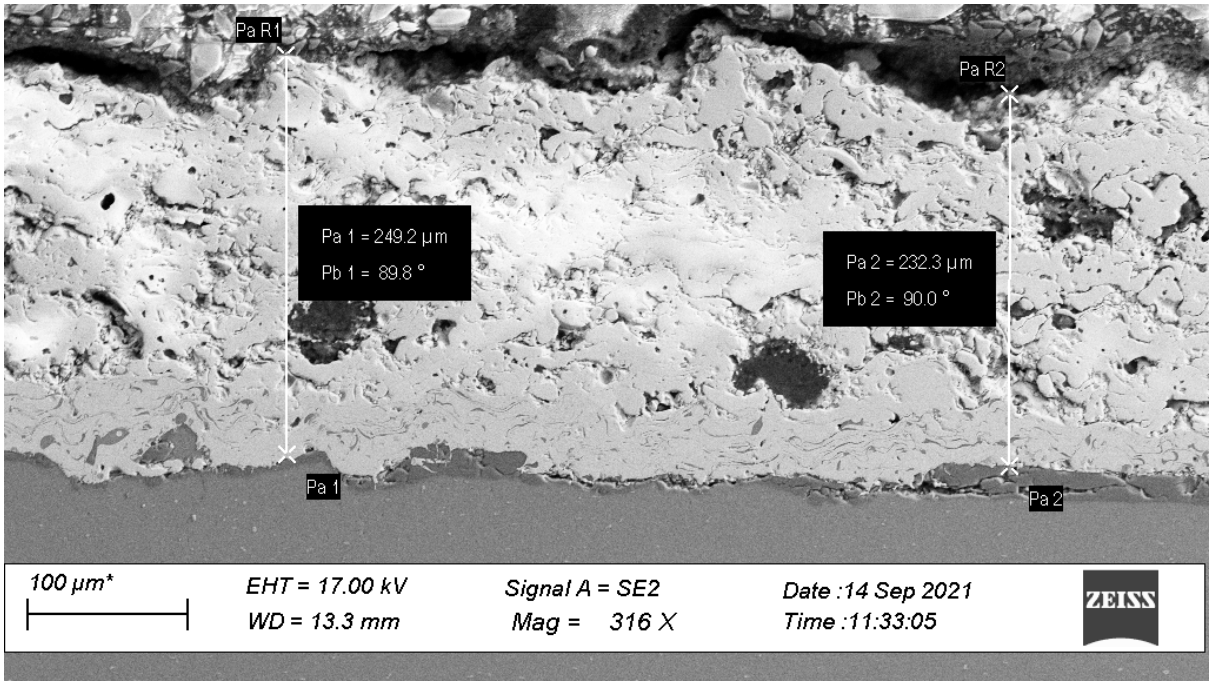

Figure 23: SEM image showing APS coating on aluminum substrate of sample APS1

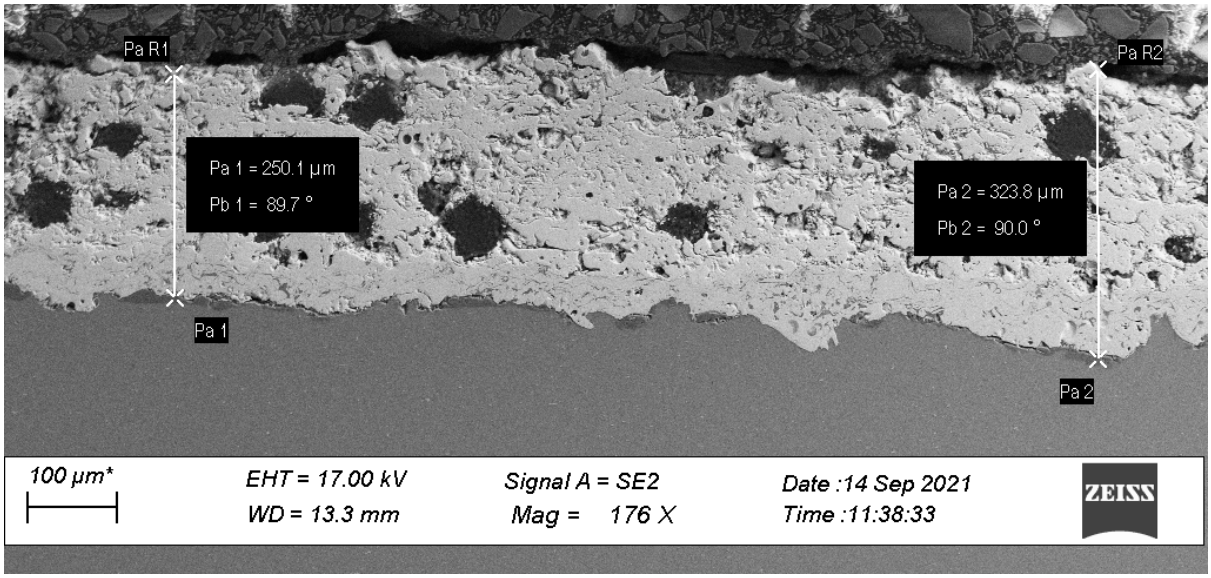

Figure 24: SEM image showing APS coating on aluminum substrate of sample APS3

EDX analysis was performed on the samples to differentiate between the bond coat from the top coat and the results are shown below. Figure 25 shows the SEM image used for EDX analysis at different locations in the image. The location of the bond coat is confirmed with the presence of elements like Ni, Co, Cr, and Al (seen in Figure 26). Similarly, the location of the substrate was confirmed by the presence of elements like Al and Mg in spectrum 10 seen in Figure 28. Spectrum 8 shows the presence of Zr and Y which confirms the location of top coat seen in Figure 27.

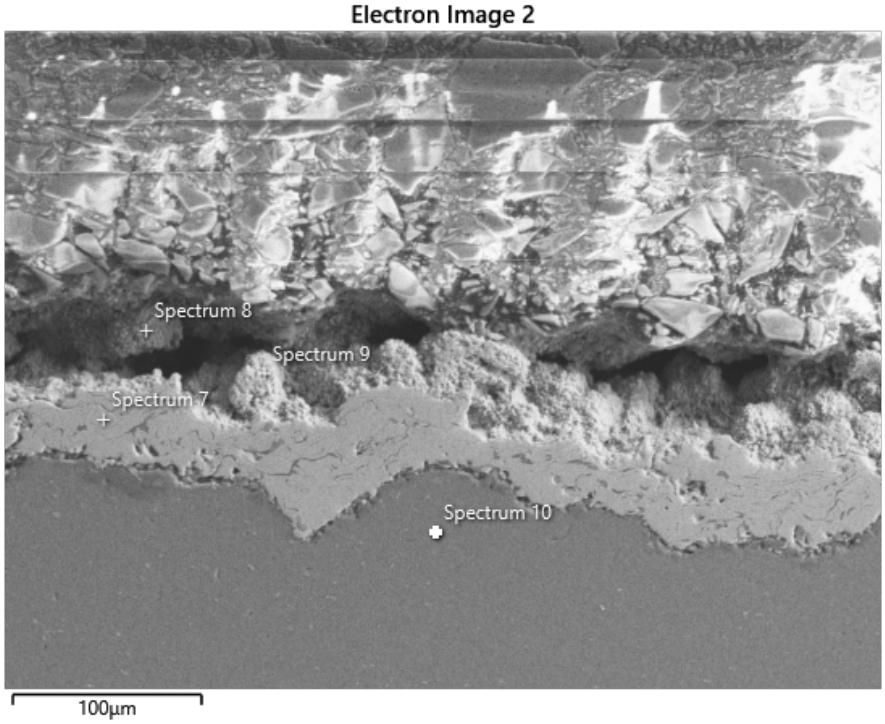

Figure 25: SEM image for EDX analysis

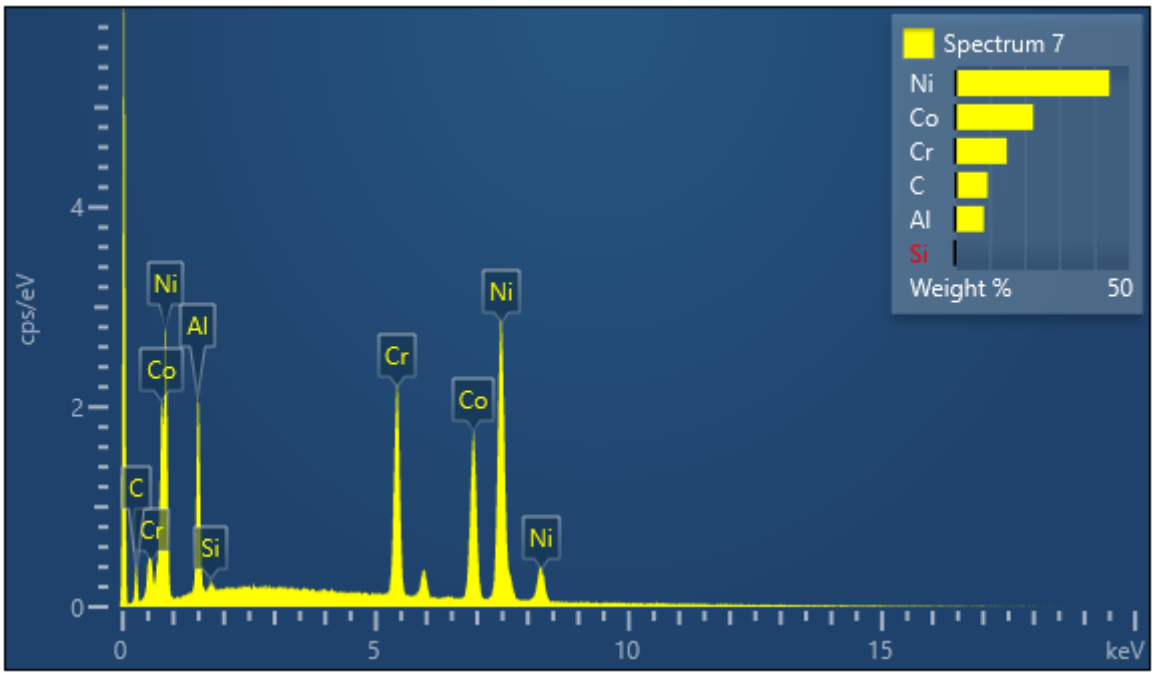

Figure 26: EDX results of spectrum 7 showing the bond coat

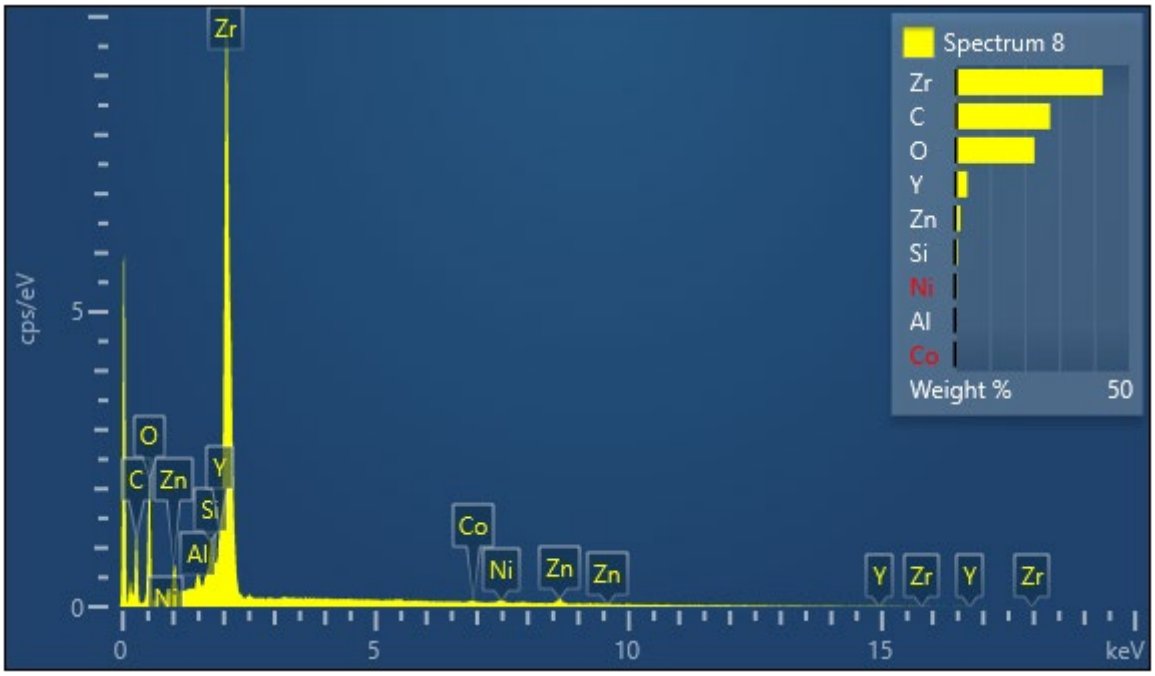

Figure 27: EDX results of spectrum 8 showing the top coat

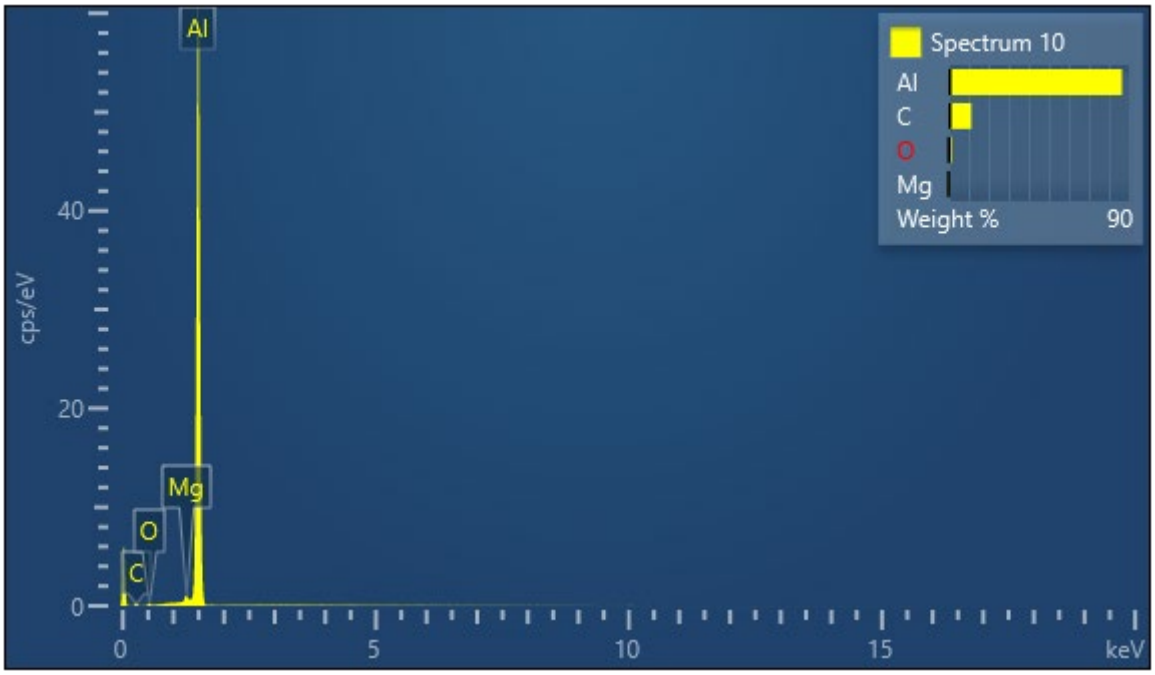

Figure 28: EDX results of spectrum 10 showing the substrate

9.2 Mechanical Testing

Drop weight test was performed to crack the coating present on the aluminum substrate and to study the propagation of the crack in two different coatings. The cracked coatings were analyzed in stereo microscope. Figure 29 and Figure 30 shows the cracked coating of APS and SPS, respectively. For a load of 1000 g dropped from a height of 60 cm from the base plate, APS coating cracked, and the crack propagation was observed across an area of 6.3 mm X 5.2 mm whereas for similar conditions in SPS coating, the crack propagation was observed over an area of 10 mm X 12.5 mm. The reason for smaller area of crack is due to the presence of porosity and polymer in the coating.

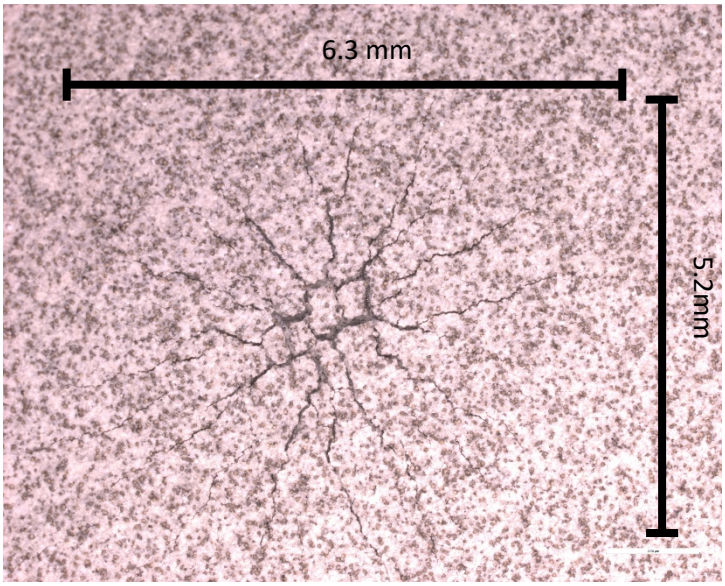

Figure 29: Cracked APS coating for a height of 60 cm and a load of 1000 g

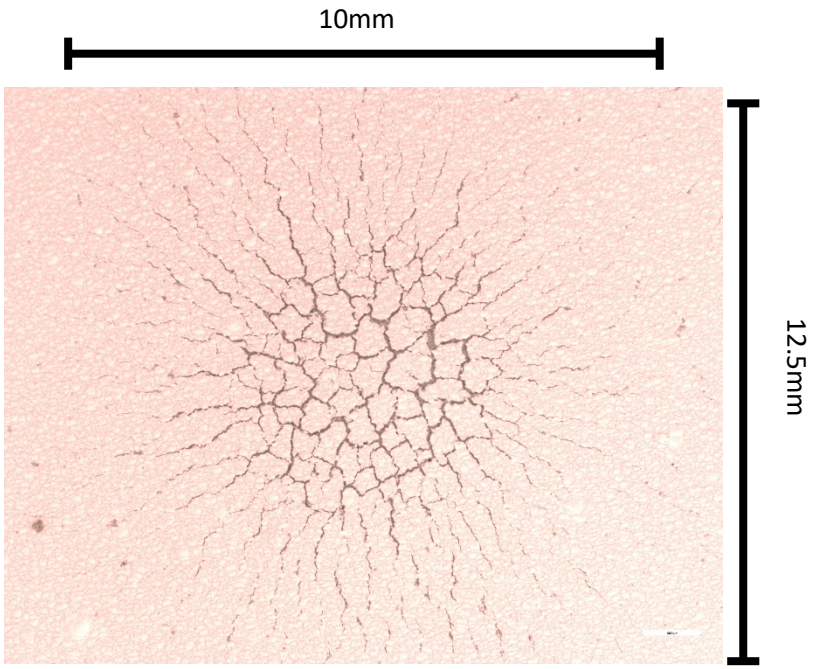

Figure 30: Cracked SPS coating for a height of 60 cm and a load of 1000 g

Figure 31 shows the crack propagation in APS, the crack has greater energy originating from the center of the crack and the energy for crack propagation dissipates as it moves away from the center. The path of crack propagation is obstructed by the porosity or the polymer seen as black dots in Figure 31. The porosity or the polymer absorbs the energy and deviates the direction of the crack tip.

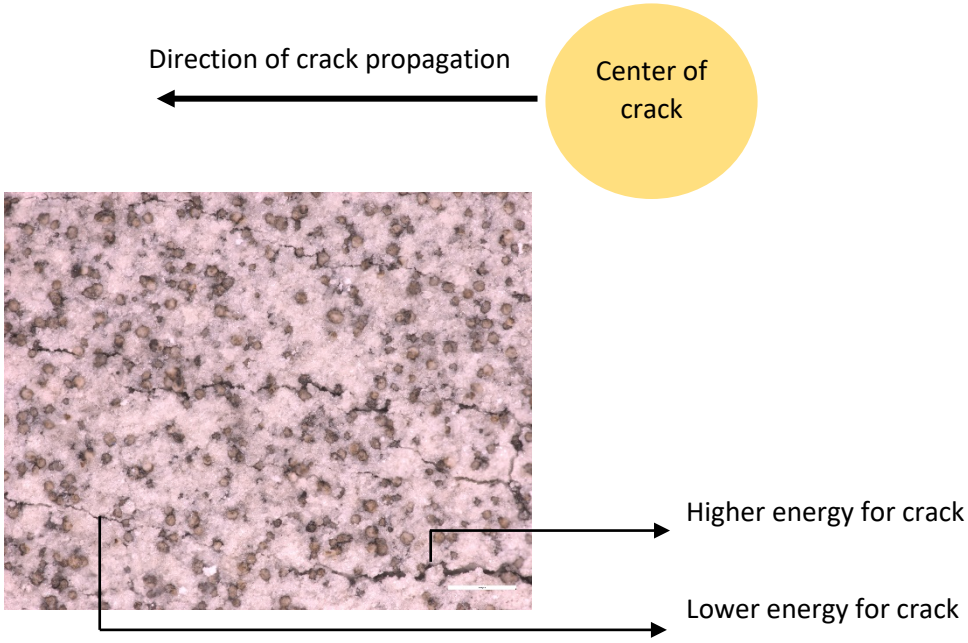

Figure 31: Crack path obstructed by polymer present in the coating

10

Conclusion

The thesis work comprises of an experimental setup to determine the effectiveness of thermal barrier coatings when used as a method to control the TR of Li-ion batteries. The two different types of coatings compared are atmospheric plasma sprayed YSZ with a polymer filling in the pores and suspension plasma sprayed YSZ both coated on an aluminium plate of thickness 3.0 mm. The experimental results shows that the APS coating performs better during mechanical loading when compared to SPS coated YSZ. The difference in the performance of the coating can be attributed to the presence of polymer in the pores of the APS coated material which restricts the growth of the crack when an impact loading is applied on the material. The SPS coated plate on the other hand has better thermal resistance. This comparison between the APS and the SPS coating is inconclusive because it is unfair to compare two different coating methods with two different matrix. Further experiments can be conducted with a polymer filling in both APS and SPS coating for a fair comparison between the coating techniques and thus we can determine if TBC can be used for prevention of TR in Li-ion batteries.

Bibiliography

1. https://ec.europa.eu/clima/policies/transport/vehicles/heavy_en
2. Nitta, N., Wu, F., Lee, J. T., & Yushin, G. (2015). Li-ion battery materials: present and future. *Materials today*, *18*(5), 252-264.
3. Feng, X., Ren, D., He, X., & Ouyang, M. (2020). Mitigating thermal runaway of lithium-ion batteries. *Joule*, *4*(4), 743-770.
4. Beauregard, G. P. (2008). Report of investigation: Hybrids plus plug in hybrid electric vehicle. *US Department of Energy, Idaho National Laboratory, Idaho Falls, ID, Report*, (5903).
5. B. Smith, Chevrolet volt battery incident overview report 1, U.S. Department of Transportation, National Highway Traffic Safety Administration, 2012.
6. Aircraft incident report: auxiliary power unit battery fire, Japan airlines Boeing 787, JA 829 J, Boston, Massachusetts, January 7, 2013. National Transportation Safety Board, DC, Rep. No. PB2014-108867, Nov. 21, 2014.
7. N. Goto, Aircraft serious incident investigation report: all Nippon airways Co. Ltd. JA804A. Japan Transport Safety Board, Tokyo, Japan, Rep. No. AI2014-4, Sep. 25, 2014.
8. Miao, Y., Hynan, P., Von Jouanne, A., & Yokochi, A. (2019). Current Li-ion battery technologies in electric vehicles and opportunities for advancements. *Energies*, *12*(6), 1074.
9. Wang, Q., Ping, P., Zhao, X., Chu, G., Sun, J., & Chen, C. (2012). Thermal runaway caused fire and explosion of lithium ion battery. *Journal of power sources*, *208*, 210-224.
10. Scrosati, B., & Garche, J. (2010). Lithium batteries: Status, prospects and future. *Journal of power sources*, *195*(9), 2419-2430.
11. Shurtz, R., & Hewson, J. C. (2016). *UNDERSTANDING THE LIMITS OF THERMAL RUNAWAY IN LITHIUM-ION BATTERY SYSTEMS* (No. SAND2016-9331C). Sandia National Lab.(SNL-NM), Albuquerque, NM (United States).
12. Heiskanen, S. K., Kim, J., & Lucht, B. L. (2019). Generation and evolution of the solid electrolyte interphase of lithium-ion batteries. *Joule*, *3*(10), 2322-2333.

13. Yang, H., Amiruddin, S., Bang, H. J., Sun, Y. K., & Prakash, J. (2006). A review of Li-ion cell chemistries and their potential use in hybrid electric vehicles. *Journal of industrial and engineering chemistry*, *12*(1), 12-38.
14. Alaoui, C. (2012). Solid-state thermal management for lithium-ion EV batteries. *IEEE Transactions on Vehicular Technology*, *62*(1), 98-107.
15. Viswanathan, V. V., Choi, D., Wang, D., Xu, W., Towne, S., Williford, R. E., ... & Yang, Z. (2010). Effect of entropy change of lithium intercalation in cathodes and anodes on Li-ion battery thermal management. *Journal of Power Sources*, *195*(11), 3720-3729.
16. Chen, D., Jiang, J., Kim, G. H., Yang, C., & Pesaran, A. (2016). Comparison of different cooling methods for lithium ion battery cells. *Applied Thermal Engineering*, *94*, 846-854.
17. Wang, T., Tseng, K. J., Zhao, J., & Wei, Z. (2014). Thermal investigation of lithium-ion battery module with different cell arrangement structures and forced air-cooling strategies. *Applied energy*, *134*, 229-238.
18. Wang, T., Tseng, K. J., & Zhao, J. (2015). Development of efficient air-cooling strategies for lithium-ion battery module based on empirical heat source model. *Applied Thermal Engineering*, *90*, 521-529.
19. Monika, K., Chakraborty, C., Roy, S., Dinda, S., Singh, S. A., & Datta, S. P. (2021). Parametric investigation to optimize the thermal management of pouch type lithium-ion batteries with mini-channel cold plates. *International Journal of Heat and Mass Transfer*, *164*, 120568.
20. Kim, G. H., & Pesaran, A. (2007). Battery thermal management design modeling. *World Electric Vehicle Journal*, *1*(1), 126-133.
21. Li, W. Q., Qu, Z. G., He, Y. L., & Tao, Y. B. (2014). Experimental study of a passive thermal management system for high-powered lithium ion batteries using porous metal foam saturated with phase change materials. *Journal of power sources*, *255*, 9-15.
22. Wang, Z., Zhang, Z., Jia, L., & Yang, L. (2015). Paraffin and paraffin/aluminum foam composite phase change material heat storage experimental study based on thermal management of Li-ion battery. *Applied Thermal Engineering*, *78*, 428-436.
23. Babapoor, A., Azizi, M., & Karimi, G. (2015). Thermal management of a Li-ion battery using carbon fiber-PCM composites. *Applied Thermal Engineering*, *82*, 281-290.
24. Bose, S. (2017). *High temperature coatings*. Butterworth-Heinemann

25. Nicholls, J. R., Simms, N. J., Chan, W. Y., & Evans, H. E. (2002). Smart overlay coatings—concept and practice. *Surface and Coatings Technology*, *149*(2-3), 236-244.
26. Thibblin, A. (2019). *Thermal Barrier Coatings for Heavy-Duty Diesel Engines* (Doctoral dissertation, KTH Royal Institute of Technology).
27. Guazzato, M., Albakry, M., Ringer, S. P., & Swain, M. V. (2004). Strength, fracture toughness and microstructure of a selection of all-ceramic materials. Part II. Zirconia-based dental ceramics. *Dental materials*, *20*(5), 449-456.
28. Krella, A. K. (2016). Degradation of protective PVD coatings. In *Handbook of Materials Failure Analysis with Case Studies from the Chemicals, Concrete and Power Industries* (pp. 411-440). Butterworth-Heinemann.
29. Wiecinski, P., Smolik, J., Garbacz, H., Bonarski, J., Mazurkiewicz, A., & Kurzydłowski, K. J. (2017). Microstructure and properties of metal/ceramic and ceramic/ceramic multilayer coatings on titanium alloy Ti6Al4V. *Surface and Coatings Technology*, *309*, 709-718.
30. Hwu, K. L., & Derby, B. (1999). Fracture of metal/ceramic laminates—II. Crack growth resistance and toughness. Acta materialia, 47(2), 545-563.
31. Mahade, S. (2018). Functional performance of gadolinium Zirconate/Yttria stabilized zirconia multi-layered thermal barrier coatings (Doctoral dissertation, University West).
32. Łatka, L. (2018). Thermal barrier coatings manufactured by suspension plasma spraying-a review. *Advances in Materials Science*, *18*(3), 95-117.
33. Yüksel, N. (2016). The review of some commonly used methods and techniques to measure the thermal conductivity of insulation materials. In *Insulation materials in context of sustainability*. IntechOpen.
34. Ponton, C. B., & Rawlings, R. D. (1989). Vickers indentation fracture toughness test Part 1 Review of literature and formulation of standardised indentation toughness equations. *Materials science and technology*, *5*(9), 865-872.
35. Dorfman, M. R. (2018). Thermal spray coatings. In Handbook of environmental degradation of materials (pp. 469-488). William Andrew Publishing.

DEPARTMENT OF INDUSTRIAL AND MATERIALS SCIENCE
CHALMERS UNIVERSITY OF TECHNOLOGY
Gothenburg, Sweden 2021
www.chalmers.se

CHALMERS
UNIVERSITY OF TECHNOLOGY